Surveys in Geophysics
https://doi.org/10.1007/s10712-025-09899-3

Signatures of Polar Vortex Weakening in the MLTI: A Review

V. L. Harvey[1] · D. Aggarwal[2] · E. Becker[3] · M. Bittner[4,5] · B. Funke[6] · L. Goncharenko[7] · J. Jia[8] · R. Lieberman[9] · H.-L. Liu[10] · V. Maliniemi[11] · A. Marchaudon[12] · H. Nesse[13] · N. Partamies[14] · N. Pedatella[10] · C. Schmidt[4] · G. Shi[15,16] · C. C. Stephan[17] · G. Stober[15,16] · W. van Caspel[18] · S. Wüst[4] · Y. Yamazaki[17]

Received: 24 February 2025 / Accepted: 25 July 2025

Abstract

This paper is a collaborative effort that originated at the International Space Science Institute Workshop on "Physical links between Weather and Climate in Space and the Lower Atmosphere" held 22–26 January 2024. Many scientists attended that workshop and contributed their expertise related to polar vortex impacts on upper atmosphere variability. This paper summarizes well-known and newly reported signatures of polar vortex weakening on mesosphere–lower-thermosphere (MLT) temperature, winds, composition, planetary waves, gravity waves, tides, and ionospheric foF2. A variety of observational and modeling results are shown and are consistent with previously published variations in the dynamical and chemical state of the MLT and ionosphere during weak vortex events. We present Superposed Epoch Analysis (SEA) of upper atmosphere diagnostics and phenomena where day 0 is the onset of major SSWs. We also present SEAs where day 0 is the onset of stratopause warmings followed by elevated stratopause events. Our goal in performing two SEAs is to test the sensitivity of 10 hPa versus 1 hPa winds to predict upper atmosphere variability. Results suggest that zonal winds and the semidiurnal migrating solar tide (SW2) in the MLT are more sensitive to zonal wind reversals at 1 hPa rather than 10 hPa. Alternatively, the non-migrating DW2 tide in the equatorial upper mesosphere is best predicted by planetary wave-1 amplitudes in the winter high-latitude upper stratosphere rather than zonal wind reversals. A notable aspect of both SEAs is extremely large event-to-event variability in all diagnostics. Thus, conclusions drawn based on any one event are less robust than those based on many events.

Keywords Polar vortex · Sudden stratospheric warming · Planetary wave · Gravity wave · Atmospheric tide · Atmospheric coupling

Article Highlights

- This paper summarizes upper atmosphere responses to polar vortex weakening
- Superposed Epoch Analyses are performed for 10 hPa and 1 hPa zonal wind reversals, testing their predictive skill for upper atmosphere variations

---

Extended author information available on the last page of the article

- Zonal winds and semidiurnal migrating tides in the lower thermosphere appear to be more strongly linked to zonal wind reversals at 1 hPa than at 10 hPa
- There is significant event-to-event variability in upper atmosphere responses to vortex weakening, underscoring the need for multi-event analyses to draw robust conclusions

1 Introduction

The polar vortex forms in the winter stratosphere and mesosphere as a result of reduced solar insolation and less diabatic heating due to the absorption of UV radiation by ozone (Schoeberl et al. 1992). These conditions create a cold polar stratosphere and, through the thermal wind relationship, generate a west-to-east jet stream in mid-latitudes, which surrounds the cold air at high latitudes. During winter, the polar vortex serves as a vertical coupling agent in the atmosphere, connecting the upper atmosphere to the middle atmosphere from the top down via descending nitrogen oxides from the mesosphere and lower thermosphere (MLT) to the stratosphere (e.g., Randall et al. 2009). Moreover, the vortex connects the state of the stratosphere to lower altitudes through the downward transmission of stratospheric circulation anomalies into the troposphere (Baldwin and Dunkerton 2001). The polar vortex also connects the atmosphere–ionosphere system from the bottom up, influenced by planetary wave (PW)–mean flow interactions (Andrews 1985), PW effects on atmospheric tides (e.g., Forbes 1995; Goncharenko et al. 2010), and the generation and modulation of gravity waves (GWs) (e.g., Sato and Yoshiki 2008; Becker and Vadas 2018; Becker et al. 2022a; Vadas et al. 2024a, b). The polar vortex extends into the mesosphere (Harvey et al. 2018), but, unfortunately, most coarse (~2°) global models exhibit large zonal mean zonal wind biases in the polar winter upper mesosphere (Harvey et al. 2022a) that preclude its accurate representation in the upper mesosphere. Harvey et al. (2022b) argue that this model deficiency must be remedied to enable accurate forecasts of the ionosphere and space weather.

When wintertime quasi-stationary planetary Rossby waves forced in the troposphere (hereafter: quasi-stationary PWs) are weak, the stratospheric part of the polar vortex is nearly radiatively driven and thus is nearly zonally symmetric and pole centered. Quasi-stationary PWs and GWs are key drivers of the middle atmosphere's residual circulation, which results in a temperature structure that deviates from radiative equilibrium (Holton 1983). Since GWs deposit momentum where they dissipate, westward momentum forcing associated with GW dissipation, reaching tens of m/s/day, drives the mesospheric branch of the residual circulation in the winter hemisphere. The so-induced downwelling in the mesosphere over the polar region leads to adiabatic heating and thereby a "separated" polar winter stratopause (Hitchman et al. 1989) within the polar vortex core (Duck et al. 1998), a feature that would not occur in the polar night in the absence of westward wave driving in the mesosphere. Conversely, GW-driven ascent in the summer mesosphere results in temperatures at the summer mesopause that are the coldest on the planet (Lindzen 1981).

Sudden Stratospheric Warmings (SSWs) are extreme disruptions to the polar vortex driven by upward propagating quasi-stationary PWs forced in the troposphere and are associated with rapid warming of the polar stratosphere (Matsuno 1970; see also review by Baldwin et al. 2021 and references therein). During SSWs, the polar stratosphere can warm by tens of degrees Kelvin in a few days and the climatological westerly zonal winds in mid-latitudes weaken or reverse direction in response to the warming. These zonal wind changes result in a strong reduction or even a slight reversal of the westward GW drag in the upper mesosphere (orographic and non-orographic), which acts to weaken the mesospheric branch of the residual circulation and leads to cooling in the polar upper mesosphere (e.g., Siskind et al. 2010). Indeed, mesospheric cooling during SSWs has long been observed (e.g., Quiroz 1969; Labitzke 1972) and simulated in models (e.g., Cho et al. 2004; Liu and Roble 2002). Siskind et al. (2010) go on to describe the sequence of events during prolonged SSWs. In response to mesospheric cooling, a strong westerly mesospheric polar vortex forms, which allows westward-propagating non-orographic GWs to reach the upper mesosphere. During this SSW recovery phase, the westward GW drag from these GWs drives strong westward accelerations and polar descent that results in the transport of trace gases from the MLT to the stratosphere (e.g., Orsolini et al. 2017 and references therein) and adiabatic heating that can form an “elevated stratopause” (ES) (Manney et al. 2008; Manney et al. 2009).

During SSWs, changes in the zonal winds in the stratosphere give rise to changes in the propagation of PWs, GWs, and tides that are communicated upward into the mesosphere, thermosphere, and ionosphere. Fast traveling PWs are enhanced during SSWs and propagate up into the thermosphere where they modulate the winds, solar and lunar tides, and neutral densities (e.g., McLandress et al. 2006; Yue et al. 2021). The westward Eliassen-Palm flux divergence from strongly enhanced quasi-stationary PWs during SSWs drives anomalous upwelling and cooling at low latitudes (Yulaeva et al. 1994) that enhances tropical stratospheric ozone (Randel 1993) which, in turn, contributes to the amplification of the migrating semidiurnal tide (SW2) in the winter MLT (e.g., Limpasuvan et al. 2016; Siddiqui et al. 2019). Enhancements to SW2 and the migrating semidiurnal lunar tide (M2) are known to influence the dynamo generation of electric fields in the E-region (e.g., Pedatella et al. 2014). While quasi-stationary PWs are enhanced during SSWs, it is well known that stratospheric and mesospheric GW activity is drastically reduced (e.g., Harvey et al. 2023 and references therein). Thus, it is not surprising that Frissell et al. (2016) determined medium-scale traveling ionospheric disturbances (believed to be driven, in part, by GWs) to also be reduced during SSWs.

Pedatella et al. (2018b) discuss how the state of the polar vortex has far-reaching effects, from impacts on surface weather (Kidston et al. 2015), to variations in polar mesospheric clouds at the summer polar mesopause (Karlsson et al. 2009; Smith et al. 2020; Lieberman et al. 2021), perturbations in temperature that extend pole to pole and from the stratosphere to the thermosphere (Miyoshi et al. 2015; Randel 1993; Limpasuvan et al. 2016; Karlsson & Becker 2016), anomalous global circulation patterns in the mesosphere and lower thermosphere (Laskar et al. 2019; Miyoshi et al. 2015), altered stratosphere/mesosphere composition (e.g., Randall et al. 2009; Tweedy et al. 2013), and thermospheric composition (Oberheide et al. 2020), changes in thermospheric density (Stober et al. 2012; Yamazaki et al. 2015), and variations in ionospheric parameters (e.g., Chau et al. 2012; Goncharenko et al. 2010, 2021a). And while this list is long, it is not exhaustive. Anomalies of opposite sign appear when the polar vortex is anomalously strong (Pedatella and Harvey 2022), though this is beyond the scope of this work.

This paper employs superposed epoch analysis (SEA) of multiple weak vortex events to summarize known variability in MLT temperatures, neutral winds, composition, PWs, GWs, tides, and newly reported variations in ionospheric foF2. We organize a variety of observations into the SEAs, namely, ground-based IR spectrometers and microwave radiometers, SuperDARN and meteor radars (MRs), MLS, SABER, MIPAS, and COSMIC-2 satellite data, and ionosondes. We also include whole atmosphere model results from the Whole Atmosphere Community Climate Model with thermosphere-ionosphere eXtension (WACCMX), the Navy Operational Global Atmospheric Prediction System (NOGAPS)

Advanced Level Physics High Altitude (ALPHA), and the Upper Atmosphere ICosahedral Nonhydrostatic (UA-ICON) model. The outline of the paper is as follows. Section 2 describes how we categorized the data with respect to either major SSW onset date or the onset of stratopause warmings followed by ES events. Sections 3–8 present analysis of the following diagnostics with respect to disturbance onset date: (3) MLT temperature, (4) stratosphere/mesosphere composition, (5) GWs, (6) neutral horizontal wind and PWs, (7) tides, and (8) F-region SW2 and foF2 variability. Section 9 discusses how the polar vortex, SSWs, and vertical coupling may change in future climate scenarios. Conclusions are given in Sect. 10.

2 SSW Classification and SEA Analysis

To quantify SSW-induced variability in the atmosphere–ionosphere system, one must first objectively define SSW onset date. For decades, "major" and "minor" SSW definitions involve the reversal of zonal mean zonal winds at 60°N and 10 hPa and reversed temperature gradients from 60° to 90°N at 10 hPa, respectively (e.g., McInturff 1978; Butler et al. 2017; Harvey et al. 2022a). However, SSW definitions have changed over the years and remain somewhat ambiguous in their implementation (Butler et al. 2015). For example, Baldwin and Dunkerton (2001) presented compelling results of composite strong and weak "extreme stratospheric events" and their impact on tropospheric weather based on Northern Annular Mode index values. Charlton and Polvani (2007) classified SSWs based on the shape and structure of the polar vortex rather than binary zonal wind and temperature gradient diagnostics. Yet others have found it useful to define disturbances to the polar vortex near the stratopause (~ 50 km) rather than at 10 hPa (~ 30 km) (e.g., Tweedy et al. 2013; Stray et al. 2015; Limpasuvan et al. 2016).

In this work, we define major SSWs to occur when the zonal mean zonal winds at 60°N and 10 hPa reverse in the Modern Era Retrospective analysis for Research and Applications version 2 (MERRA-2, Bosilovich et al. 2015; Molod et al. 2015; Gelaro et al. 2017). Sixteen major SSWs were identified from 1998 to 2024. Dates from 1998 to 2019 match those presented in Butler et al. (2017) and Harvey et al. (2022a). We define "stratopause warmings" followed by ES events to occur using the three selection criteria presented in Stray et al. (2015). Namely, when there is (1) mesospheric cooling (MLS $T < 185$ K at 80 km), (2) a reversal of MERRA-2 zonal mean zonal winds at 1 hPa that persists for 5 days or more, and (3) the polar cap average stratopause altitude jumps over 10 km in the vertical (see also Tweedy et al. 2013). While Stray et al. required zonal winds to reverse for only 4 days, we require 5 days to match major SSW criteria. This selection criteria identified 15 such events from 1995 to 2024. Dates from 1995 to 2013 match those presented in Limpasuvan et al. (2016). Table 1 gives onset dates of major SSWs (left column) and "stratopause warmings" followed by ES events (middle column) since 1995 that are used in this work. There are 9 events where major SSWs and stratopause warmings followed by ES's occur in conjunction. In these cases, stratopause warming onset occurs from 0 to 18 days before SSW onset. This lag is expected given the known downward propagation of circulation anomalies (e.g., Baldwin and Dunkerton 2001). There are 6 stratopause warming/ES events that do not have a corresponding major SSW. These cases highlight that the SSW definition does not capture disturbances to the vortex that are confined to the upper stratosphere and lower mesosphere. Likewise, there are 7 SSWs without an associated stratopause warming/ES. In these cases, the vortex disturbance was confined to the lower

Table 1 Onset dates of major SSWs (left column), stratopause warmings followed by ES events (middle column), and events observed by SABER, MLS, and MIPAS (right column)

Major SSW onset	U < 0 @ 1 hPa and ES	Satellite observations
	24 Jan 1995	
	19 Dec 1997	
15 Dec 1998	13 Dec 1998	
26 Feb 1999	22 Feb 1999	
	10 Dec 2000	
11 Feb 2001	29 Jan 2001	
	22 Dec 2001	
18 Jan 2003		S, MIPAS
	19 Dec 2003	S, MIPAS
7 Jan 2004		S, MIPAS
21 Jan 2006	8 Jan 2006	S, MLS, MIPAS
24 Feb 2007		S, MLS, MIPAS
22 Feb 2008		S, MLS, MIPAS
24 Jan 2009	21 Jan 2009	S, MLS, MIPAS
9 Feb 2010	22 Jan 2010	S, MLS, MIPAS
	13 Jan 2012	S, MLS, MIPAS
7 Jan 2013	5 Jan 2013	S, MLS
12 Feb 2018	12 Feb 2018	S, MLS
2 Jan 2019	1 Jan 2019	S, MLS
5 Jan 2021		S, MLS
16 Feb 2023		S, MLS
16 Jan 2024		S, MLS

S = Sounding of the Atmosphere using Broadband Emission Radiometry (SABER); MLS = Microwave Limb Sounder; MIPAS = Michelson Interferometer for Passive Atmospheric Sounding

stratosphere and either the zonal winds did not reverse at the stratopause or an ES did not form. The right column indicates that, during the 20-year period considered in this paper, SABER, MLS, and MIPAS observed 13, 11, and 7 major SSWs and 8, 7, and 5 stratopause warmings with ESs, respectively.

We then performed two Superposed Epoch Analysis (SEA), centered on either major SSW onset or the onset of stratopause warmings followed by ESs. Our motivation for performing two SEAs is to determine the sensitivity of disturbance altitude on SSW-induced variability in the MLTI. We performed the SEAs on a variety of observed and modeled diagnostics in the MLTI and present those results next.

3 Temperature Variations in the Stratosphere–Mesosphere–Lower Thermosphere (SMLT)

First, we show SEAs in upper mesospheric temperature as observed by ground-based airglow spectrometers that are part of the Network for the Detection of Mesospheric Change (NDMC, https://ndmc.dlr.de). The instruments receive radiation that is emitted by rotationally and vibrationally excited hydroxyl (OH*) molecules that form a layer typically at 85–87 km with a full width at half maximum of 5–7 km (annual averages, for more details concerning latitudinal and longitudinal dependence seeWüst et al. (2017, 2020). The received signal is therefore an average over the OH layer. An overview of OH airglow observations for investigating atmospheric dynamics including basics on the formation of the OH layer and the temperature retrieval from OH airglow measurements can be found in Wüst et al. (2023).

We start by looking at upper mesospheric OH temperatures at a high northern latitude site. Kjell Henriksen Observatory in Svalbard (78.2°N, 16°E), Norway hosts an Ebert-Fastie spectrometer, which has been operational since the early 1980s (Herlingshaw et al. 2025; Sigernes et al. 2003). These spectral measurements are performed throughout the dark winter season, which extends from the beginning of November until the end of February and covers most events listed in Table 1. The spectrometer scans the full spectrum of the OH (6–2) vibrational band from 830 to 879 nm in 25 s. These spectra are then averaged into 1 h and 1-day resolutions to enhance the signal-to-noise ratio. The averaged spectra are then used to estimate the neutral or kinetic temperature at the height of the OH airglow layer. The temperature estimation assumes that the rotational states of OH are in local thermodynamic equilibrium, giving rise to fine structure in the infrared emissions from the relaxation of the vibrational states of OH*. This fine structure can be used to infer the temperature. Ratios of individual emission line intensities of the OH (6–2) band are fit to a temperature-dependent synthetic spectrum, which outputs the temperature for the best fit (Sigernes et al. 2003). For selecting good fits for further analysis, we follow the procedures described by Holmen et al. (2014) and Enengl et al. (2021).

Since the polar winter upper mesosphere experiences large dynamical variations, much of the measured temperature variability is due to horizontal advection and adiabatic heating and cooling induced by waves as the airglow layer is advected upward and downward (e.g., Dyrland et al. 2010). Here, we use the daily averaged airglow temperatures to study mesopause dynamics associated with the major SSWs (10 hPa zonal wind reversals) and 1 hPa wind reversal events followed by an ES. We present SEAs to analyze the upper mesospheric temperature behavior with the zero epoch placed at SSW onset (Fig. 1, left panel) or at the onset of the easterly winds at 1 hPa (Fig. 1, right panel), both with the epoch time of ± 20 days. Individual events included in both cases are dictated by data availability. We first examined each event individually to only include the cases where the data coverage is sufficient to describe the mesopause temperature evolution around day 0. In addition to the

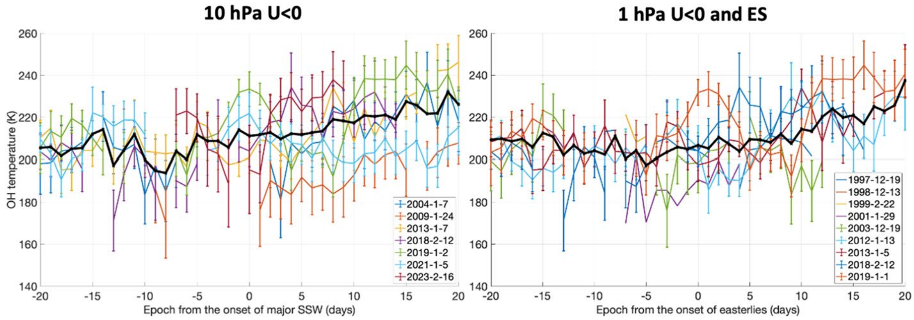

Fig. 1 Timeseries of daily mean OH temperature at Svalbard (78.2°N, 16°E) at 87 km centered on onset dates of (left) major SSWs from 2004–2023 and (right) 1 hPa zonal wind reversals followed by ES events from 1997–2019. Thick black lines are multi-event averages. Vertical lines indicate 1 standard deviation in the raw data (which are not available for the first 4 events in the right plot)

daily average temperature values, we include the standard deviation (STD) of the temperature over the averaged time period (one day). These STD values are displayed as vertical bars in Fig. 1.

The temperature time evolution over the investigated epoch periods shows large variability (up to about 20 K), which stems from the dynamically active conditions in the winter polar mesosphere. This is true within the individual events as well as for event-to-event variability. In both SEAs, coherent behavior is observed during the 20-day period after onset when all events except 2021 show a gradual warming of 20–30 K. This warming trend is not a seasonal variation since cooling is expected at this altitude moving from winter into spring. This warming trend after the SSW is likely due to enhanced GW-driven descent in the polar winter upper mesosphere as a result of primary westward GWs propagating to the upper mesosphere when a strong polar vortex is re-established after the SSW (e.g., Orsolini et al. 2017).

Next, we show SSW-induced upper mesospheric temperature variability at five NDMC sites that span 38–69°N latitude (Fig. 2). Identical infrared spectrometers, in this case following a Czerny-Turner setup and called GRIPS (GRound based Infrared P-branch Spectrometer, Schmidt et al. (2013)), are used for this purpose. These airglow observations have been available since mid-2009, thus cover up to 7 SSWs, but most sites were put into operation in later years. At the Arctic Lidar Observatory for Middle Atmosphere Research (ALOMAR/ALR: 69.3°N, 16°E), the only high-latitude site, only the 2013 SSW was observed. The measurements at the Environmental Research Station Schneefernerhaus, Germany (UFS: 47.4°N, 11°E), are available for the years 2009–2023, at Wuppertal, Germany (WUP: 51.3°E, 7.2°E), 2015–2023, at the Observatoire de Haute-Provence, France (OHP: 43.9°N, 5.7°E), 2012–2023, at Catania, Italy (CAT: 37.5°N, 15.0°E), 2011–2023. GRIPS measures radiation in the range of 1.5–1.6 µm, and neutral or kinetic temperature is retrieved following the same physical principals as described above but using different mathematics and the OH(3–1) vibrational band. Temperature values are available every 10–15 s under cloudless and dark conditions. Compared to high latitudes, measurements at mid-latitudes are, in principle, available year-round. The representativeness of the nightly mean values used for this study is investigated in Schmidt et al. (2023).

Figure 2 shows the development of upper mesospheric temperatures ± 40 days around the onset of recent major SSWs at the 5 sites given above that form a chain from Norway to Italy. The panels are organized from top to bottom in descending latitude order. The evolution of ~ 87 km temperature at ALR (69°N) displays a general warming trend following the 2013 SSW that is likely a signature of enhanced polar mesospheric descent, as was seen at Svalbard. Temperature timeseries at mid-latitude sites generally show a cooling trend in the month following SSW onset and the magnitude of this cooling increases equatorward. Some of this cooling trend may be seasonal variability, especially for years with mid-February SSWs (2010, 2018, 2023). However, this cooling is also consistent with the known out-of-phase temperature changes in low to mid-latitudes compared to high latitudes during an SSW (Randel 1993, see their Fig. 8; Limpasuvan et al. 2016, see their Fig. 7). The anomalous temperature patterns are driven by anomalous meridional circulation cells illustrated by Miyoshi et al. (2015, see their Fig. 6).

Next, we show SEAs for major SSWs and stratopause warmings followed by ESs in polar cap average MLS temperatures. The MLS data record spans August 2004 to the present and provides ~ 3500 vertical profiles each day that cover the globe (Waters et al. 2006). In this paper we use the most recent version 5 temperature, carbon monoxide (CO), and geopotential height (GPH) data throughout the stratosphere and mesosphere (Livesey et al. 2020). The version 5 temperatures are similar to previous versions (Livesey et al. 2020);

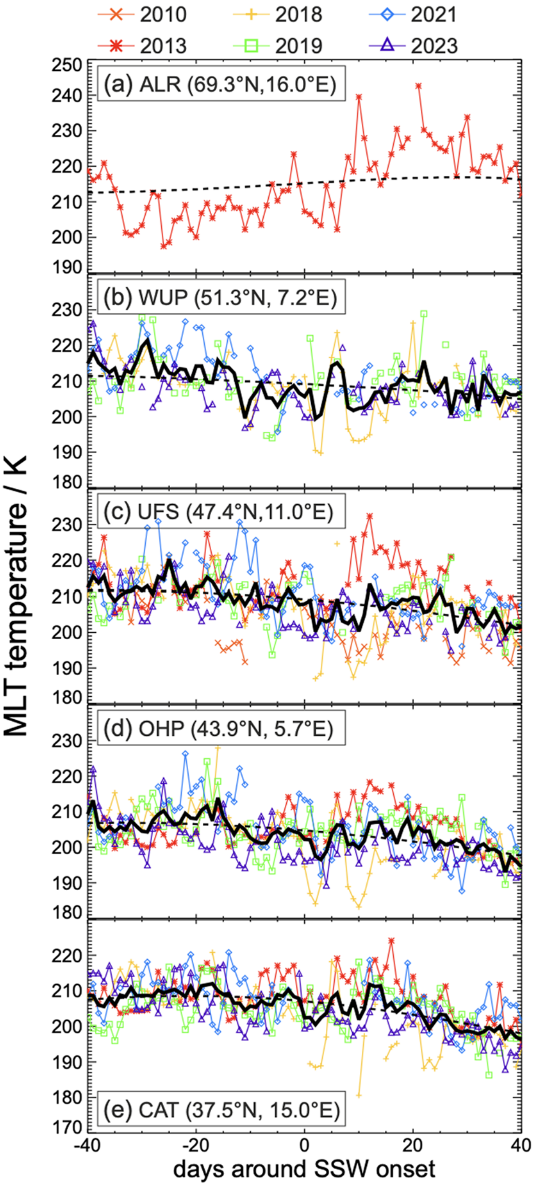

Fig. 2 Timeseries of ~ 87 km temperatures ± 40 days around the onset of recent SSWs at 5 NDMC sites from 37–69°N. Colors denote individual SSWs given in the top legend. The thick black line is the mean of all SSWs. The dotted line is the general trend

the version 2.2 products are described by Schwartz et al. (2008). From 10 to 0.001 hPa, MLS temperature profiles have a vertical resolution of 4–12 km and an accuracy of 1–3 K (Livesey et al. 2020). Estimates of precision (and accuracy) for individual GPH profiles range from 45 m (+ 100 m) at 1 hPa to 110 m (450 m) at 0.001 hPa (Livesey et al. 2020). CO is retrieved from radiances detected in the 240 GHz band and is described by Pumphrey et al. (2007) and Livesey et al. (2008). In the mesosphere, the vertical resolution of the CO data is 5–7 km and Livesey et al. (2020) indicate 20–50% positive biases, a slight improvement over previous versions (Froidevaux et al. 2006).

Figure 3 shows polar cap averaged MLS temperature (colors) from the tropopause to the mesopause for a SEA centered on major SSW onset (left) and for a SEA centered on stratopause warming onset followed by an ES (right). Gray contours are MLS CO, a tracer of wintertime descent. SEAs are given for ± 30 days from onset. Vertical profiles to the right of the altitude–time plots are individual event correlations between temperatures at 30 km and temperatures at other altitudes. All events in Table 1 that occurred from 2006 to 2024 are included. Note this analysis differs from the results shown in Figs. 1 and 2 at ground-based instrument locations in that temperatures are averaged over a large spatial domain (70°–90°N). Moreover, showing only the composite average makes it possible to see the altitude structure but it obscures event-to-event variability, which was shown to be large in Figs. 1 and 2. These results reveal the following: Before day 0, the stratopause warming SEA (right) reveals a colder stratosphere and warmer stratopause compared to the SSW SEA (left). During individual events (not shown), 30 km temperature exhibits larger variability in the month before major SSW onset compared to stratopause warming/ES onset. The 30 km temperature maximizes on SSW day 0 (left) and ES day + 2 (right). In both SEAs, mesospheric (~ 80 km) cooling occurs nearly simultaneously as the stratospheric warming. In both SEAs, lower mesospheric (~ 60 km) temperature is highly anticorrelated with 30 km temperature. In general, mesospheric cooling during SSWs is consistent with the known out-of-phase temperature changes in the stratosphere during SSWs (e.g., Labitzke 1972; Limpasuvan et al. 2016). Maximum stratospheric warming, descent of the stratopause, and mesospheric cooling generally occur in the week prior to SSW onset (left) and in the week following stratopause warming onset (right). Both SEAs show evidence of a warmer mesosphere (~ 80 km) 10–30 days after onset and CO contours that bend downward, indicative of enhanced mesospheric descent. This warming is consistent with the high-latitude observations shown in Fig. 1 and the top panel of Fig. 2. Near the peak stratospheric warming the rapid upward-sloping CO contours are likely driven by PW-driven horizontal mixing of mid-latitude air into the polar region. From 60 to 80 km, the upward sloping CO contours coincident with mesospheric cooling are likely due to ascent in the polar region driven by eastward propagating GWs.

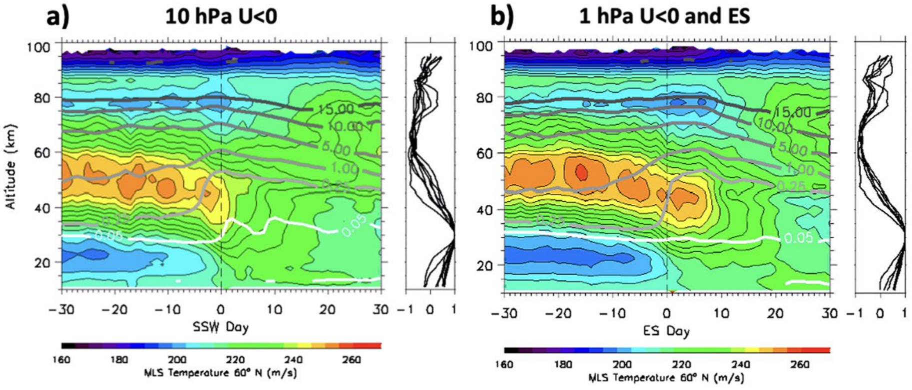

Fig. 3 Altitude–timeseries of daily mean MLS derived zonal wind (color fill) and PW 1 + 2 amplitudes (white to gray contours) at 60°N centered on onset dates of **a** major SSWs from 2004–2023 and **b** 1 hPa zonal wind reversals followed by ES events from 2006–2019. Vertical black profiles to the right of the plots give correlation coefficients between zonal winds at 30 km and zonal winds at all other altitudes for all events considered

4 Composition Variations

This section presents SSW-induced variability in SMLT composition. Shown in Fig. 4 are timeseries of SABER polar cap averaged ozone (O_3), atomic oxygen (O), atomic hydrogen (H), and temperature (T) anomalies (deviations from climatology) near 92 km during 7 stratopause warmings followed by ES events (2006–2019). At this altitude, O is an O_3 source and H is an O_3 sink. In general, O_3 changes are anticorrelated with H changes, which implies when T and O changes are similar, H is driving the O_3 changes. Both O and H have long lifetimes in MLT and can be used as indicators for vertical transport (see e.g., Brasseur and Solomon 2005; Smith et al 2010; Jones et al. 2020). Results show large event-to-event variability, especially near onset date with large anomalies of both signs.

Tweedy et al. (2013) diagnosed SSW impacts on the secondary ozone maxima near 97 km in the specified dynamics (SD) version of WACCM. They constructed a SEA from 6 SSWs, 3 of which (2006, 2009, 2010) are common to our collection of 7. They found low H was transported upward (associated with the mesospheric cooling event) that led to increased O_3 abundances in the days following onset. This behavior was pronounced during the 2010 SSW, during which our results show similar decreases in H and increases in $O_{3.}$ However, the mean SEA based on SABER observations shown here does not demonstrate reduced H and enhanced O_3 as 2010 is offset by opposing conditions during other events.

In the 2 weeks following onset, O, H, and T variations are correlated, and mean values increase due to descent. The mean temperature increases around day + 5 and does not

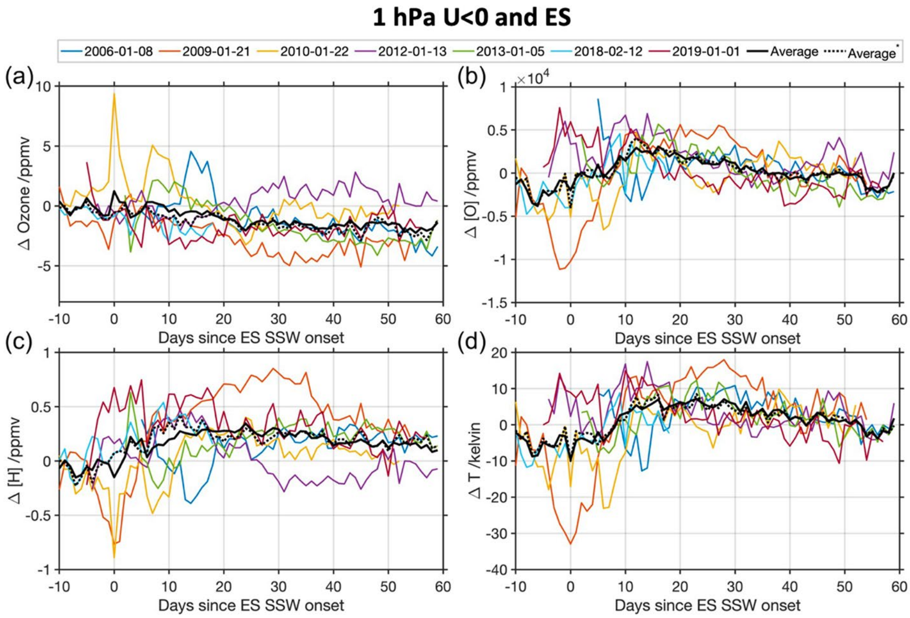

Fig. 4 Relative daily variation (data minus daily climatology) of nighttime zonally averaged ozone (O_3), atomic oxygen (O), atomic hydrogen (H), and temperature (T) at 0.0015 hPa, over the 70°–90°N latitude range, for seven ES-SSW events derived from SABER observations (colored lines). The black solid line represents the mean across the seven events, while the black dashed line denotes the median. The daily climatology is based on data from 2002 to 2019

return to pre-warming values even after 30 days. This is consistent with the warmer mesosphere observed by MLS and the airglow spectrometers after the warming. Mean increases in T and H are consistent with mean decreases in O_3, and these results agree with the findings of Tweedy et al. (2013). Interestingly, the ES-induced O_3 decreases and H increases are very long lasting and do not return to pre-SSW values even after 60 days. While springtime cooling is not obvious in the evolution of temperature, this result warrants more work to quantify a possible seasonal contribution.

Next, we show MIPAS temperature, CH_4, CO, and NO_y observations as Funke et al. (2014). NO_y is calculated as $[NO_y] = [NO] + [NO_2] + [HNO_3] + [HNO_4] + [ClONO_2] + 2[N_2O_5]$, where brackets indicate volume mixing ratios (VMR) and where N_2O_5 was counted twice to account for its two nitrogen atoms. Daily zonal means are calculated from the average of individual MIPAS profiles within 70–90°N, weighted with the cosine of the latitude. Here we use the Institute of Meteorology and Climate Research (IMK) in cooperation with the Instituto de Astrofísica de Andalucía (IAA)-processed MIPAS data version 8 which includes, compared to previous versions, a new radiometric calibration and updates in the retrieval scheme (Kiefer et al. 2021; Funke et al. 2023a, b; Glatthor et al. 2024).

Figure 5 shows timeseries of MIPAS v8 70–90°N zonal mean temperature, CH_4, CO, and NO_Y at stratospheric (30 km) and mesospheric (68 km) altitudes for (left panels) major SSW events (2003–2010) aligned with day 0 equal to major SSW onset (− 10 to + 60 days) and for (right panels) 1 hPa wind reversals followed by ESs. Timeseries are shown for individual SSWs (instead of height vs. time composites) to highlight the large event-to-event variability.

The overall conclusions from this analysis are (1) there is significant event-to-event variability in stratospheric and mesospheric temperature and trace gas responses to both

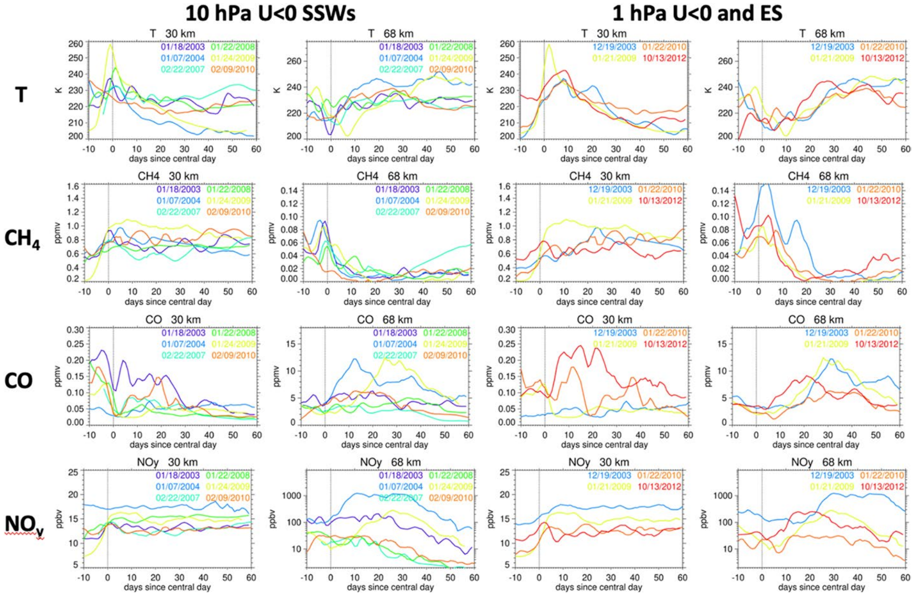

Fig. 5 Timeseries of MIPAS v8 70–90°N zonal mean temperature, CH_4, CO and NO_Y at stratospheric (30 km) and mesospheric (68 km) altitudes for (left panels) major SSW NH winters (2003–2010) aligned with the central day of the SSW (− 10 to + 60 days) and for (right panels) 1 hPa wind reversals followed by ESs for NH winters (2003–2010). Events during 2006 are excluded due to sparse MIPAS data

major SSWs and stratopause warmings followed by ESs, and (2) there are similarities in the mesospheric responses during/following the events in 2004 and 2009, as has been previously reported. Temperature variability (top panels) shows stratospheric warming and mesospheric cooling near day 0, but there is significant spread in the timing of maximum and minimum temperatures. Moreover, some years show no distinct warming at 30 km (2007 and 2010) or cooling at 68 km (2008) and we hypothesize that maximum and minimum temperature anomalies occur at different altitudes during these years. During the recovery phase (day + 10 to + 60), minimum stratospheric temperatures and maximum mesospheric temperatures occur, consistent with previous results.

Tracer variability shows both stratospheric mixing by quasi-stationary PWs and mesospheric descent. For CH_4, there is a sustained increase after day 0 in the stratosphere (in-mixing of lower latitude air) and peak values centered on day 0 in the mesosphere (descent). Note the signature of the final warming in the mesosphere in the major SSW SEA from day + 20 to + 40 to + 60 in 2007. For CO, there is a short-lived decrease around day 0 in the stratosphere during some years and a strong mesospheric enhancement in the recovery phase. In both SEAs, the magnitude and timing of the enhanced mesospheric CO after the warming are highly variable. NO_y in the stratosphere behaves similar to CH_4 due to rapid in-mixing of higher mid-latitude concentrations, especially in 2009. In the mesosphere NO_y is similar to CO and is also modulated by solar activity. Note the larger NO_y values in 2004 due to the preceding Halloween solar proton event (SPE); in that year the effect of in-mixing is less pronounced since the SPE generated NO_y over a large (50–90°N) latitude range.

Next, we examine SSW-induced variations in stratospheric and mesospheric ozone and water vapor observed by a ground-based microwave radiometer in the Arctic polar region. Ozone and water vapor are essential climate variables that play a crucial role in the absorption of solar radiation and the excitation of tides. The University Bern operates the GROMOS-C (Ground-based Ozone Monitoring System for Campaigns) and MIAWARA-C (the MIddle Atmospheric WAter vapour RAdiometer for Campaigns) radiometers at the polar station of Ny-Alesund (78.9°N, 11.9°E) to provide continuous measurements of ozone and water vapor in the Arctic polar region. Both instruments have the capability to run autonomously under extreme environmental conditions (Straub et al. 2012; Schranz et al. 2018; 2019). Since 2015, GROMOS-C and MIAWARA have been deployed at Ny-Alesund and have operated there for the past 10 years.

Figure 6 (top panels) shows a SEA of 4 major SSW events from 2018 to 2023 (12 February 2018, 2 January 2019, 5 January 2021, and 16 February 2023) for ozone and water vapor VMR and the corresponding anomalies (bottom panels) compared to the climatology (Shi et al. 2023). The VMR of both trace gases is dominated by wave driven atmospheric transport. The ozone VMR is low prior to about day -3. During SSW events, large amplitude quasi-stationary PWs lead to strongly enhanced horizontal mixing, that is, an exchange of polar ozone depleted air masses with ozone-rich air from the mid-latitudes (Schranz et al. 2020; Shi et al. 2024). The corresponding sudden increase in ozone VMR at day 0 is clearly visible in the SEA. The water vapor in the upper stratosphere exhibits an increase within 10 days of SSW onset, likely due to increased mixing of moist air from mid- and low latitudes. These increases are prolonged and last for weeks to a month or more (for ozone). Water vapor in the mesosphere then decreases from 10 to 50 days after the SSW event due to descent of dry air from the upper to the lower mesosphere. These composite results nicely summarize mean behavior, however, recall the large event-to-event variability shown in the previous SABER and MIPAS results is obscured.

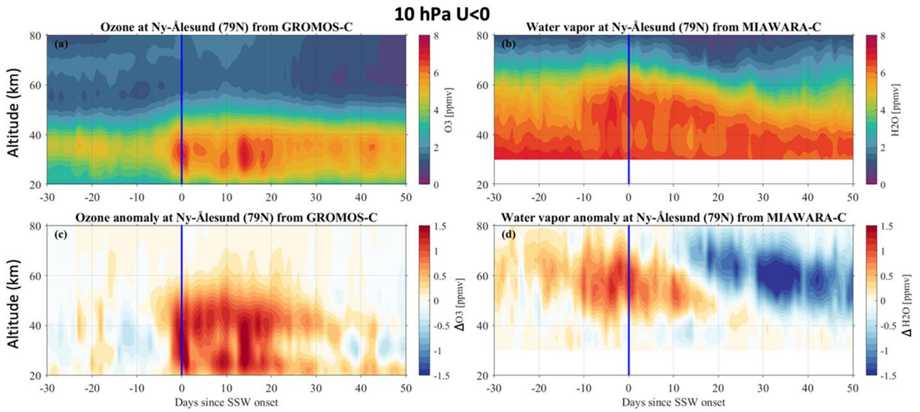

Fig. 6 Altitude–time SEAs of GROMOS-C ozone (upper left) and MIAWARA-C water vapor (upper right) volume mixing ratio for all major SSW events between 2015 to 2023. The lower panels show the ozone and water vapor volume mixing ratio anomalies (deviations from the climatology)

5 GW Variations

Turning our attention to variations in GWs during SSWs, we next examine GW forcing during the 2024 SSW in the SD-WACCMX. The upper tropospheric and stratospheric polar night jets associated with polar vortex are important source regions of inertial and mesoscale GWs, shown both in observational and modeling studies (e.g., Fritts and Nastrom 1992; O'Sullivan and Dunkerton 1995; Zhang 2004; Plougonven and Zhang 2014; Sato and Yoshiki 2008; Vadas et al. 2023, 2024a). Various mechanisms and theoretical models have been proposed to explain GW generation, including the spontaneous adjustment emission mechanism (Plougonven and Zhang 2014; see Appendix B in Becker et al. 2022b). In recent years, the increasing resolution of global models, especially whole atmosphere models, has lent further insights into the generation, propagation and dissipation of GWs. One robust feature seen in observations and numerical simulations is the strong GW activity level in the stratosphere and mesosphere, extending from the east coast of North America, across the North Atlantic Ocean, and to western Europe when the Arctic vortex is strong (e.g., Ern et al. 2011; Trinh et al. 2018; Becker et al. 2022b; Harvey et al. 2023; Liu et al. 2024). This feature is also evident in the numerical study by O'Sullivan and Dunkerton (1995) and has been tied to the upper tropospheric jet exit region. Vadas et al. (2024a) showed that this GW hot spot in the wintertime middle atmosphere includes significant contributions from primary GWs generated by spontaneous emission in region of the stratospheric polar vortex jet.

The stratosphere polar vortex is disrupted during SSWs. GW activities display large variation during SSWs, with strong GW decreases in the stratosphere and mesosphere after the onset of SSWs (e.g., Harvey et al. 2023), and increases during the vortex recovery phase, as seen in COSMIC observations (Yamashita et al. 2010). Such variations have been reproduced in high-resolution global models (Yamashita et al. 2010; Liu 2017; Becker et al. 2022a). The variations could result from a combination of changes in GW generation by the polar vortex and/or secondary GW sources, GW generation from the tropospheric sources during SSW, and GW filtering by the large-scale winds (e.g., Liu 2017; Becker et al. 2022b, a; Zhang et al. 2025).

Global models with coarse resolution and parameterized GW forcing can capture GW filtering and wave impacts on the circulation in the MLT during and following SSWs. However, it has been noted that the MLT response during the SSW recovery phase differs from observations. For example, during the recovery phase, the ES descends much faster in simulations than in observations (Pedatella et al. 2018a).

Figure 7a–b compares the simulated temperature averaged over the polar region (70°–90°N) in coarse resolution SD-WACCMX (0.9° × 1.25° horizontal resolution) with parameterized GW forcing to high-resolution SD-WACCMX (~0.25° horizontal resolution) without parameterized GW forcing during January 2024. Both simulations show a minor SSW in the first half of the month, followed by a major SSW (17 January onset, with peak warming on 20 January). The time variation in the mesospheric temperature structure, however, is quite different between the two. The mesospheric responses in the high-resolution simulation during the minor warming and following the major warming appear to be more gradual, and the decay of the mesospheric cooling region is much slower, which is in better qualitative agreement with MLS observations of this SSW (not shown). Following the major SSW, the upper mesosphere in the high-resolution simulation is warmer than in the coarse simulation, implying stronger descent in the high-resolution run.

Figure 7c–d compares the zonal forcing by parameterized GWs (lower left) and the zonal forcing by resolved GWs (zonal scale < 2000 km, lower right) at 60°N. The two are

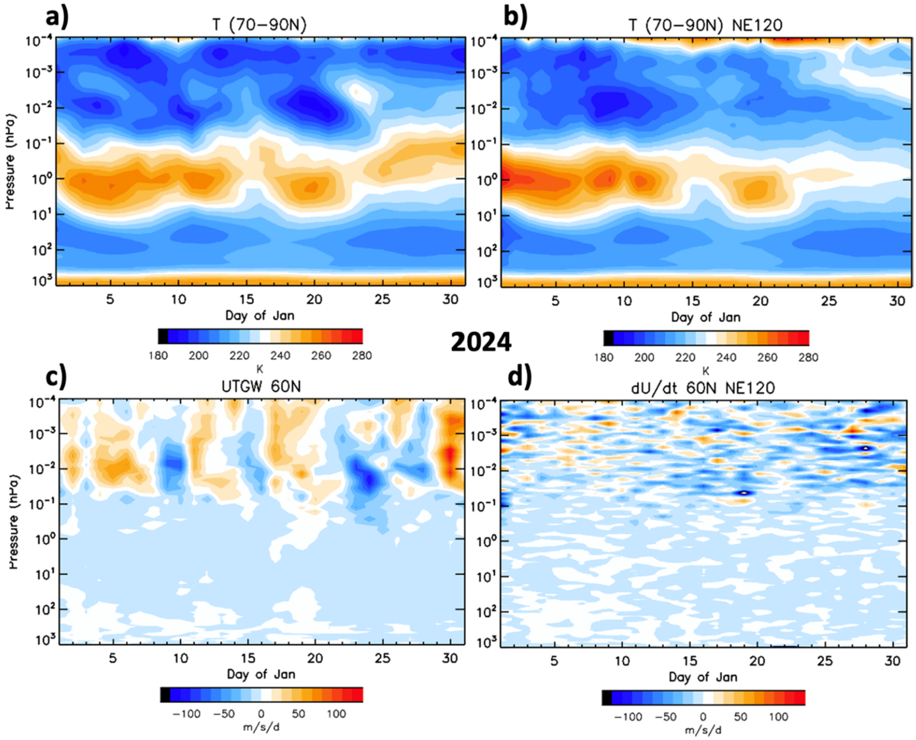

Fig. 7 Altitude–timeseries for January 2024 of polar mean temperature in a) coarse resolution SD-WACCMX b) high-resolution SD-WACCMX. Altitude-timeseries for January 2024 of zonal mean zonal forcing by c) parameterized GWs in coarse resolution SD-WACCMX and d) resolved GWs (zonal scale < 2000 km) in high-resolution SD-WACCMX

vastly different. The parameterized GW forcing responds immediately to the zonal wind change in the stratosphere, and it is more uniform in the mesosphere and lower thermosphere. On the other hand, the zonal forcing by resolved GWs is significantly more variable in altitude and time. The more gradual response of the temperature in the high-resolution simulation may be a consequence of the integrated effect of the variable GW forcing. The high-resolution results suggest the actual GWs and GW forcing changes during the SSW are markedly more complex than the changes in wave filtering by large-scale winds. Further work is needed to assess the fidelity of resolved GWs on SSW-induced variations in upper mesospheric temperature.

6 Neutral Wind and PW Variations in the SMLT

This section presents SSW-induced variability in SMLT neutral winds and PWs from the point of view of the MLS satellite, the SuperDARN radars, and meteor radar observations. For MLS, first the GPH data are gridded separately for both ascending and descending nodes, and the two nodes are daily averaged to reduce tidal effects. We then calculate geostrophic winds from the daily averaged GPH fields (e.g., Holton 2004, Eq. (3.11)). Precision estimates for zonal mean zonal winds are 2 m/s at 0.01 hPa (~80 km). PW amplitudes are computed at each pressure level and latitude by iteratively computing a least-squares fit of a sine wave to the MLS GPH data around each latitude circle.

Figure 8 gives altitude–time SEAs of MLS zonal wind and PW 1 + 2 at 60°N centered on major SSW onset (left) and stratopause warmings followed by ES onset (right) for all events in Table 1 from 2004 to 2024. Recall that there is large event-to-event variability embedded in these SEAs; nevertheless, the following key points can be made about the mean behavior. In the major SSW SEA (Fig. 8a), the evolution of the zonal mean zonal wind at 30 km shows a wind reversal on SSW day 0, as expected. Mean SEA zonal winds reverse in the upper mesosphere prior to major SSW day 0, though these wind values are small and likely insignificant given the large event-to-event variability. In the stratosphere

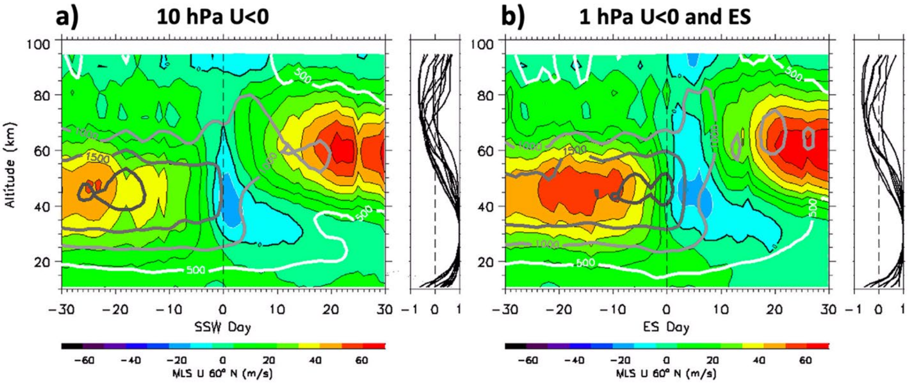

Fig. 8 Altitude–timeseries of daily mean MLS temperature (color fill) and CO (white to gray contours) averaged poleward of 70°N centered on onset dates of **a** major SSWs from 2004–2023 and **b** 1 hPa zonal wind reversals followed by ES events from 2006–2019. Vertical black profiles to the right of the plots give correlation coefficients between temperatures at 30 km and temperatures at all other altitudes for all events considered

easterlies persist, on average, 2 weeks after onset. Two weeks after onset, the polar night jet is stronger than before onset and 15–20 km higher altitude.

In the SEA of stratopause warmings followed by ESs (Fig. 8b), the polar night jet is ~ 30% stronger before onset compared to the major SSW SEA. Zonal mean zonal winds reverse simultaneously from 30 to 75 km and from 85 to 95 km on day 0. In the stratosphere easterlies persist, on average, 3 weeks after onset. In both SEAs, event-to-event variability in 30 km winds in the weeks following onset ranges from − 20 m/s to + 20 m/s (not shown). In the stratosphere, PW amplitudes maximize 2–3 weeks prior to major SSW onset (left) and one week prior to stratopause warming/ES onset. In the mesosphere near 80 km, traveling PW amplitudes maximize ~ 5 days after onset for both major SSWs and stratopause warmings with ESs, in agreement with Stray et al. (2015).

Next, we examine the evolution of zonal and meridional winds, the quasi-6-day westward zonal wavenumber-1 PW (Q6DW), and the migrating semidiurnal tide (SW2) in the upper mesosphere observed by SuperDARN. While designed to measure ionospheric E-region and F-region plasma phenomena, the network of High-Frequency (HF) SuperDARN radars also detects radio wave backscatter ("meteor echoes") from meteoric ionization trails (Chisham and Freeman 2018). These meteor echoes can be used to derive the neutral wind velocity carrying the ionization trails, which, when aggregated into hourly bins, can be used to calculate hourly mean zonal and meridional winds. The SuperDARN HF-radars are unique in that they have been operational since 1993, while also spanning a geographic area extensive enough to resolve the longitudinal structure of tides and PWs (van Caspel et al. 2020, 2022). The 10 stations used in the current work are the same as those described in van Caspel et al. (2022), spanning 180° of longitude in a 14° latitude band centered on 60°N.

The winds, SW2, and Q6DW shown in Fig. 9 are representative of a broad vertical average (80–120 km) at a single central altitude. The wave amplitudes and mean winds are determined by fitting a 6-day sliding window in both space and time across all available hourly SuperDARN measurements, with the fitting function representing the diurnal, semidiurnal, and terdiurnal migrating tides (DW1, SW2, TW3, respectively), and the Q6DW forms together with a mean wind. Including the Q6DW is motivated by recent literature describing its enhancement in the neutral wind and ionospheric system during SSWs (e.g., Liu et al. 2021; Aa et al. 2024; Ma et al. 2024). A 6-day fitting window was chosen to cover at least one full Q6DW period. Fits are performed only when at least 432 hourly wind measurements are present, corresponding to an average up-time of 75% for at least 4 stations. For brevity, in the following, wave amplitudes are only shown for the meridional wind component. We further note that our analysis did not find any noteworthy response in the DW1 or TW3 tidal waves in the SuperDARN winds, so these are not discussed.

Figure 9 shows SuperDARN SEAs of horizontal winds, SW2, and the Q6DW. In all panels, event-to-event variability is visible and SEA means are shown in black lines with solid black being the mean of the 15 stratopause warmings followed by ES events and dashed black being the mean of the 16 major SSWs at 10 hPa. Figure 9a illustrates that the zonal winds are predominantly eastward in the weeks prior to and after the disturbance, which is likely due to eastward secondary GWs (Becker et al. 2022a; Harvey et al. 2022a). In the days surrounding onset, the zonal winds shift westward in a majority of the 15 stratopause warming events followed by ESs (event dates are listed at the top), though the timing of the shift varies from event to event. Not all events see a reversal of the winds in the MLT, while for other events the zonal winds shift easterly before onset. One reason for these variations might be that the vertical averaging extent (80–120 km) spans a vertical layer in which the zonal winds change sign (e.g., Becker et al. 2022a), leading to vertical cancelation effects over the SuperDARN meteor

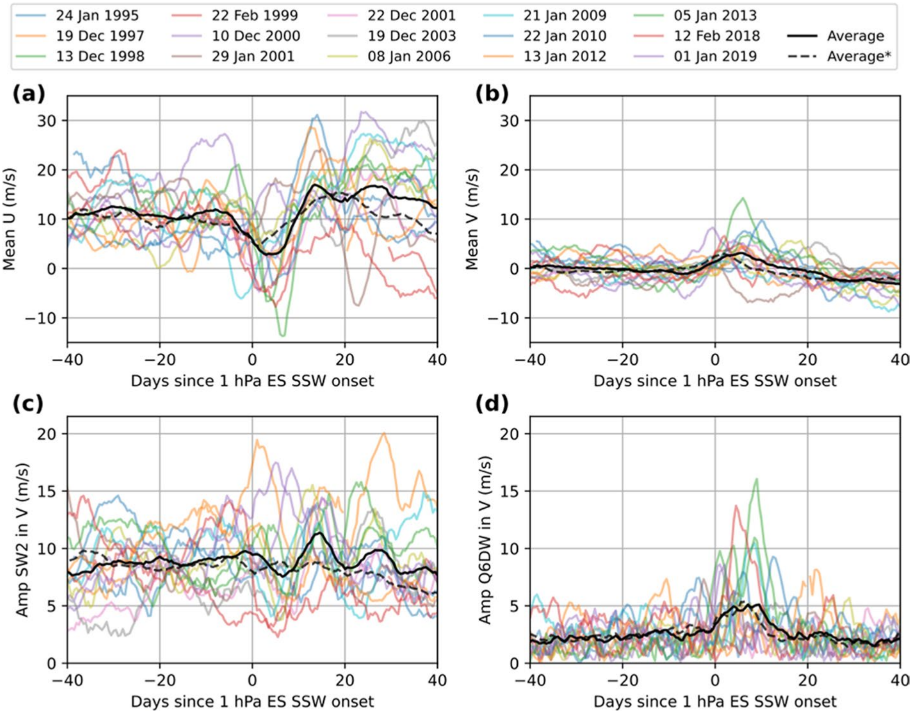

Fig. 9 SuperDARN zonal wind (**a**), meridional wind (**b**), SW2 amplitude (**c**), and Q6DW amplitude (**d**) centered on the onset dates of the 15 ES SSW events. The solid black curve shows the composite mean response. The dashed black curve shows the composite mean response when the results are centered on the 16 SSW onset dates at 10 hPa

echo range. The SEA mean shows the zonal wind in the MLT weakens 5 days prior to the onset of the wind reversal at 1 hPa and reaches a minimum on day + 5. The dashed black line indicates zonal winds in the major SSW SEA minimize earlier, in agreement with the MLS SEA between 80 and 95 km. Figure 9b shows a poleward enhancement coincident with the westward turning of the zonal wind (day 0 to day + 10). The SW2 tide results in Fig. 9c will be discussed in the next section.

The Q6DW (Fig. 9d) displays an enhancement about a week after the onset date, even though there is considerable event-to-event variability in terms of the amplitude and timing of the enhancement. We note that, while identifying the time evolution of low-frequency waves over the relatively short SSW time periods can be challenging (e.g., Stober et al. 2020; van Caspel et al. 2023), diagnostic analysis using longer time windows in combination with wave frequencies in the range of 3–8 days, does indicate that amplitudes maximize for waves with a period of ~ 6 days.

7 Tidal Variability

This section summarizes SSW signatures in migrating and nonmigrating solar tides based on SuperDARN and meteor radar, SABER, and COSMIC-2 observations and in the WACCMX, UA-ICON, and NOGAPS-ALPHA models. In SuperDARN, the mean SEA response (solid black line) in SW2 (Fig. 9c) shows diminished amplitudes on about day + 8 followed by an enhancement on about day + 15, consistent with the SuperDARN meteor wind analysis of Hibbins et al. (2019). These results are also generally consistent with the SuperDARN SEA analysis of SW2 during major SSWs by Zhang et al. (2021). While SW2 enhancements "cluster" around day + 15 for individual events, there is significant event-to-event variability in the SW2 response. The timing of the response can vary by a few days from event to event, and there is also considerable variation in SW2 amplitudes before, during, and after onset. The black dashed curves in Fig. 9 show the mean SEA response when centered on the 16 SSW onset dates at 10 hPa. While this composite response shows generally similar results, the response "signal" on day + 15 is effectively lost. This suggests that the SW2 tide might be more sensitive to wind reversals at 1 hPa rather than at 10 hPa.

Next, we look at stratopause warming SEAs in U, V, and SW2 along a chain of three altitude-resolving meteor radars (MRs) that extends from Collm (51.3°N) to Svalbard (78.2°N). MRs have become a ubiquitous tool to monitor mesospheric winds. During the past decade, the number of MRs has increased substantially and many regions in the world have been observed for almost two decades. The Svalbard MR (SVA) was commissioned in 2003 and has operated nearly continuously since 2004 providing reliable wind measurement at (78.2°N, 16°E) (Hall and Tsutsumi 2020). On the Scandinavian mainland, the Tromso MR (TRO) located at (69.59°N, 19.2°E) is one of the oldest and has collected data from 2003 until today (Hall and Tsutsumi 2013). The Collm MR (COL) was installed during summer of 2004 and has also operated continuously since then at the Collm geophysical observatory (51.3°N, 13°E) (Jacobi et al. 2007). All three MRs were upgraded over the years enhancing the altitude coverage and robustness of the derived winds. The winds are analyzed with the latest version of wind retrieval described in Stober et al. (2021a, 2022) including nonlinear error propagation, a Tikhonov regularization for the vertical winds embedded as spatio-temporal Laplace filter and WGS84 geodetic coordinates to minimize projection errors for all three wind components.

Figure 10 gives a map projection (left) of the three MR stations and altitude–time panels of the zonal winds (left), meridional winds (middle), and SW2 (in U, right) at each of the three MRs, ordered top-to-bottom from high to lower latitudes. Mean SEA wind and tidal amplitudes were derived by calculating the mean response about the central day of the following seven stratopause warming events at 1 hPa with an ES: 8 January 2006, 21 January 2009, 22 January 2010, 13 January 2012, 5 January 2013, 12 February 2018, and 1 January 2019. Non-migrating tides exhibit less phase coherence among SSW events (Stober et al. 2021b), thus, these tides are not included in the SEA tidal analysis. Note there is large event-to-event variability so caution should be used when interpreting weak winds or small tidal amplitudes. The mean SEA zonal winds reflect the typical weak eastward (positive) winds before the onset (day 0) and strong eastward winds below 95 km for 2 months after onset. The wind magnitude and altitude of the jet core increase toward the mid-latitudes, indicative of an equatorward tilting polar vortex jet. The meridional winds (middle panels) indicate the presence of PW oscillations and a tendency for the flow to be equatorward before onset. After onset, the meridional winds are consistently poleward in this European longitude sector. These mean zonal and meridional wind variations are consistent

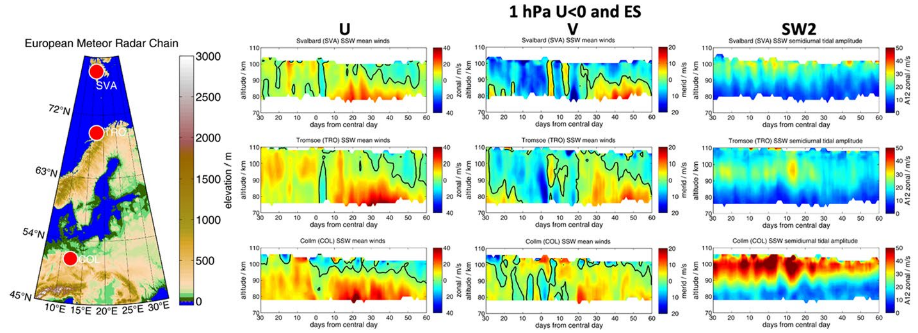

Fig. 10 Map of the European sector indicating the locations of the three meteor radars located at Svalbard (SVA), Tromso (TRO), and Collm (COL). The panels to the right show the zonal winds, meridional winds, and SW2 (U) derived from SEA of stratopause warmings with ESs that occurred between 2006 and 2019

with mesospheric cooling during and warming after onset, as shown in previous figures. The wind patterns at the mid-latitude station at Collm depend on the overall position of the polar vortex and the nature of the disturbance (vortex split vs. vortex displacement). Thus, individual events display large wind variations (e.g., Stober et al. 2020). At Tromso, there is an enhancement in SW2 amplitudes on day + 12 from 90 to 100 km; at Collm SW2 is enhanced 2 weeks before to 2 weeks after onset. The SW2 enhancement at Tromso is consistent with SuperDARN observations (60°N, Fig. 9c). Given the large event-to-event variability seen in the SuperDARN results, it is not clear whether this enhancement is significant.

Next, we perform a SEA centered on stratopause warming dates followed by ESs for the migrating diurnal (DW1), semidiurnal (SW2), and terdiurnal (TW3) tides in SABER. SABER temperature measurements (Esplin et al. 2023; Russell III et al. 1999) at 110 km were analyzed to determine the average response of migrating solar tides in the ionospheric dynamo region to the eight 1 hPa wind reversals followed by ESs listed in Table 1 from 2003 to 2019. Our method of data analysis involves two steps. In the first step, seasonal variations in the zonal mean temperature, tides, and stationary PWs were determined using a technique similar to that described by Forbes et al. (2008) and Pancheva and Mukhtarov (2011). In this step, the measurements around the onset date of polar vortex weakening (− 10 to + 20 days) were excluded to minimize their influence. The obtained seasonal variations were then subtracted from the respective measurements to derive residual temperatures. In the second step, a SEA was performed by fitting tides to 60 days of residual temperatures collected over the 8 events to evaluate variations in the migrating solar tides from their seasonal cycles.

Figure 11a–c shows latitude–time SEAs of the amplitudes of migrating solar tides in the residual temperatures observed by SABER. The lagged response of the SW2 is most prominent, which is consistent with previous studies (e.g., Jin et al. 2012; Wang et al. 2014). Also, variations are seen in DW1 preceding the SW2 response, which is in qualitative agreement with previous studies (e.g., Siddiqui et al. 2022; Hocke 2023). The response of TW3 is not as evident. Figure 11d shows that the phase of the SW2 is approximately 180° apart between the northern and southern hemispheres, indicating that this tidal component is antisymmetric about the equator. For further characterization, it is convenient to expand the SW2 component into a series of Hough modes (e.g., Forbes 1995). Figure 11e demonstrates that SW2 is well captured by the first two symmetric and antisymmetric semidiurnal

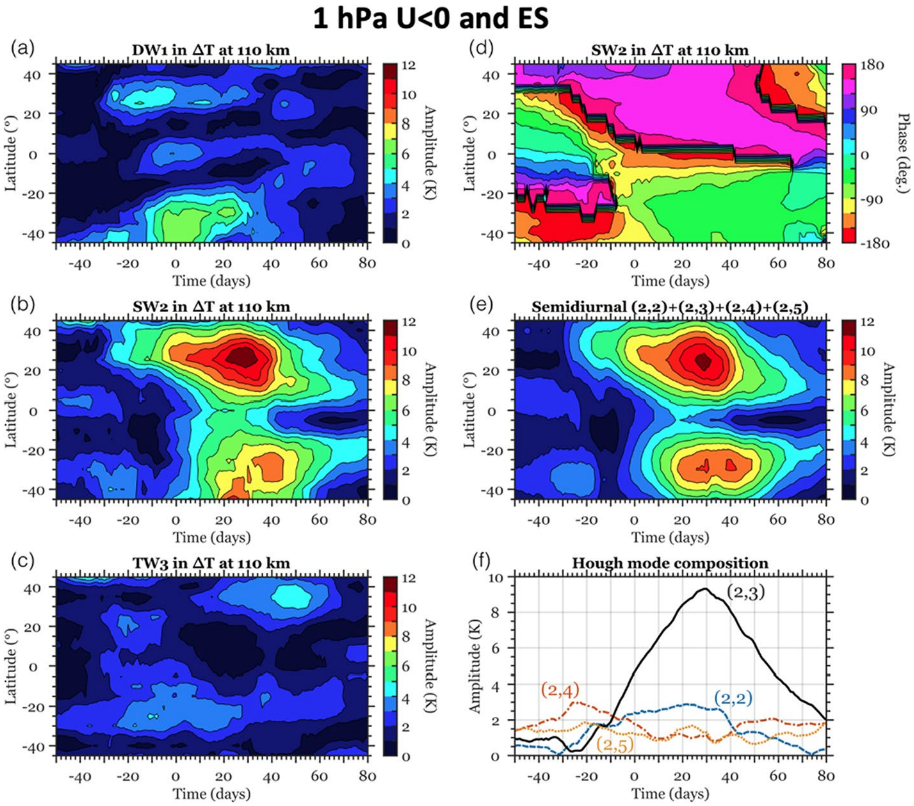

Fig. 11 Latitude–time SEAs for stratopause warming events in Table 1 from 2003–2019. **a**–**c** Amplitudes of migrating solar diurnal (DW1), semidiurnal (SW2) and terdiurnal (TW3) tides in the residual TIMED/SABER temperatures at 110 km after removal of seasonal variations in the zonal mean temperature, tides and stationary PWs. **d** Phase of SW2. **e** Reconstruction of SW2 amplitude by the semidiurnal (2,2), (2,3), (2,4) and (2,5) Hough modes. **f** Amplitude of the semidiurnal (2,2), (2,3), (2,4) and (2,5) Hough modes

Hough modes. According to Fig. 11(f), the SW2 response to polar vortex weakening can be largely explained by an enhancement of the first antisymmetric semidiurnal (2,3) mode, which agrees with previous studies (Yamazaki et al. 2012; Yamazaki and Siddiqui 2024).

Next, we present tidal responses to vortex weakening events in three different global models. While there are known differences between models with parameterized GWs and observations and between coarse and high-resolution model versions, these coarse resolution model results are useful to document as it is these model versions that are most widely used by the scientific community. Moreover, the computing expense of high-resolution simulations prevents studying multiple events with high-resolution models so low-resolution models are still needed. Figure 12 shows timeseries of coarse resolution SD-WACCMX zonal mean zonal winds at 60°N in the winter middle mesosphere, DW1 in the tropical upper mesosphere, and SW2 at 50°N in the winter lower thermosphere centered on the dates of wind reversals at 10 hPa (left column) and at 1 hPa (right column). The black lines are the SEA means. The tides are shown for locations (altitudes, latitudes) where they peak and results are similar to what has been shown in previous studies. There is clearly large event-to-event variability in the zonal

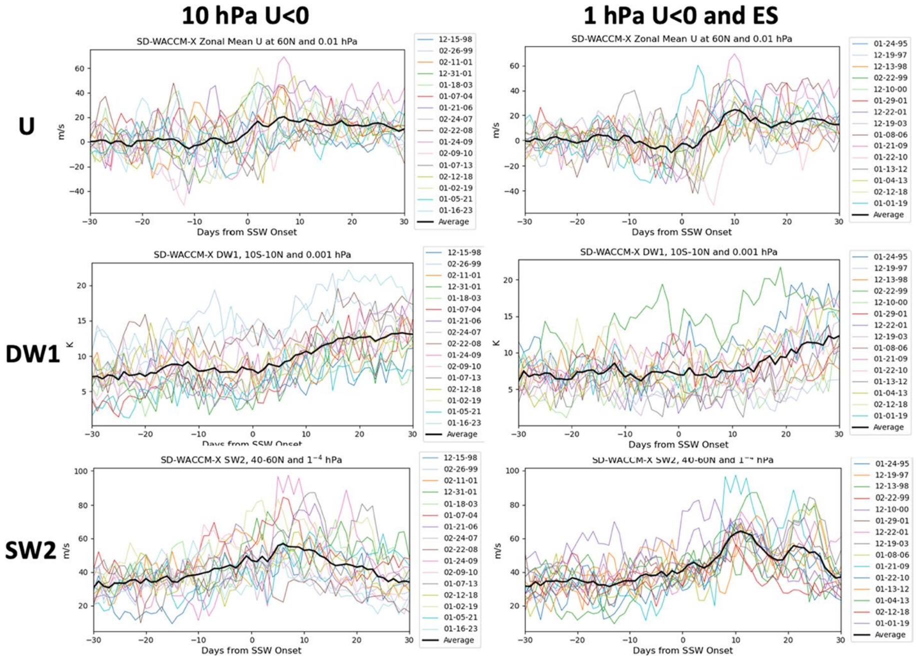

Fig. 12 Timeseries of SD-WACCMX zonal mean zonal winds at 60°N and 0.01 hPa (top row) centered on the dates of wind reversal at 10 hPa (left) and at 1 hPa (right). Corresponding plots are shown for the DW1 (in T) at the Equator and 0.001 hPa (middle row) and SW2 at 50°N and 0.0001 hPa (in U) (bottom row)

winds and both tidal components. Like the SuperDARN results, there appears to be a clearer response when SEAs are based on wind reversals at 1 hPa.

For the SEA mean in zonal mean zonal winds at 0.01 hPa (black lines), WACCMX shows a slight decrease in the zonal mean zonal winds prior to day 0 and an enhancement ~ 10 days after the central date. A stronger response is apparent when SEAs are based on central dates at 1 hPa (right column) compared to 10 hPa. The vortex weakening impact on the low-latitude DW1 is relatively weak and is primarily evident when looking at the anomalies from the climatology (not shown). Overall, DW1 decreases around the central date by ~ 1–1.5 K (~ 15–20%). The gradual DW1 increase in the month following day 0 can be partly attributed to seasonal variations, whereby DW1 maximizes at equinox (Siddiqui et al. 2022). Results at mid-latitudes show SW2 enhancements of ~ 20–30 m/s that maximize from day + 7 to day + 12. There is a second SW2 enhancement from day + 20 to day + 25 that was also observed by SuperDARN in Fig. 9c that warrants further study. This double peaked enhancement in SW2 agrees with the SD-WACCMX SEA analysis of SW2 during major SSWs by Zhang et al. (2021). The SW2 enhancements shown here are larger and show the double-peak enhancement when compositing with respect to central dates at 1 hPa compared to 10 hPa.

Next, we look at the time–altitude evolution of U and the time-latitude evolution of SW2 in the UA-ICON general circulation model (Zängl et al. 2015; Borchert et al. 2019; Kunze et al. 2024) during the 2023 major SSW. The model horizontal resolution is ~ 20 km (icosahedral grid R2B7) with 250 vertical levels that extend from the surface to the model top at 150 km. This corresponds to a vertical resolution of 600 m from 40 to 110 km. The simulation employs the non-orographic GW parameterization of Warner and McIntyre (1996) with the normalization constant of the saturation wave spectrum (C*) set to 20. The model was nudged to the 6-hourly operational analysis of the European Centre for Medium-range Weather Forecasting-Integrated Forecasting System (ECMWF-IFS) up to a height of 50 km.

The upper panel of Fig. 13 shows that the model captures the occurrence of the major SSW, as expected (due to being nudged to ECMWF). The maximum weakening of the polar vortex occurred in the model on 17 February 2023 (one day after onset in MERRA-2), with the westward zonal mean zonal wind extending from 30 to 75 km. The evolution of the zonal winds is in excellent agreement with MLS in the stratosphere and lower mesosphere, with subtle differences from 60 to 90 km (not shown). The lower panel depicts the amplitude of SW2 at 105 km. Following the polar vortex weakening, an enhancement occurred in the SW2 amplitude over mid-latitudes in both hemispheres with the maximum responses from 22 to 24 February 2023, 5–7 days after the maximum polar vortex weakening. The delayed response agrees with previous observations and models and may be partly explained by the time needed for the tidal wave to propagate from the lower atmosphere and establish a steady oscillation (e.g., Vial et al. 1991).

We next explore vortex weakening impacts on the DW2 nonmigrating tide in the NOGAPS-ALPHA model during the 2009–2010 Arctic winter. During this dynamically active winter, there was a stratopause warming event on 22 January 2010 and a major SSW event on 9 February 2010. However, results will demonstrate that PW-1 amplitude, rather than onset of zonal wind reversals, most accurately predicts DW2 behavior in the tropical MLT.

Advective processes that couple PWs with migrating tides have long been proposed as sources of nonmigrating tides in the middle atmosphere (Teitelbaum and Vial 1991;

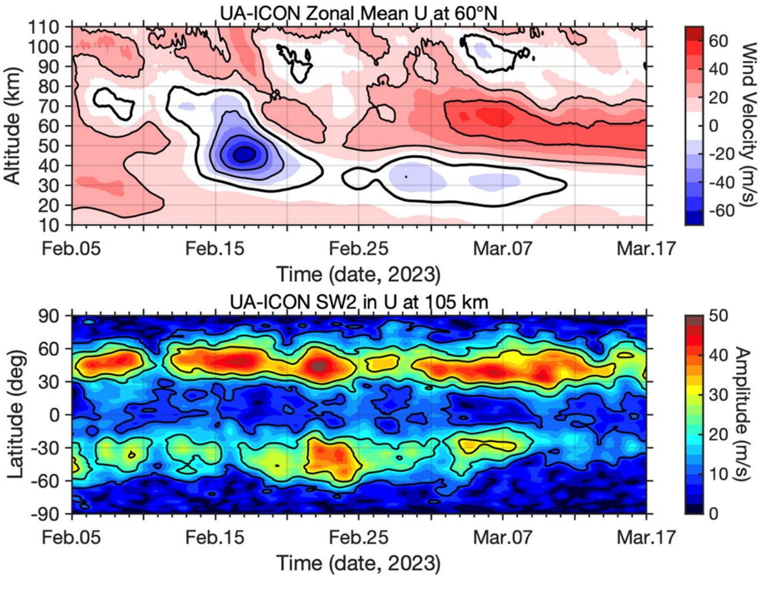

Fig. 13 (Top) Altitude–timeseries of daily mean zonal mean UA-ICON zonal wind at 60°N during the 2023 major SSW. (Bottom) Latitude–timeseries of the amplitude of SW2 in zonal wind at 105 km estimated using the technique of Yamazaki (2023)

Hagan and Roble 2001). This interaction yields secondary waves with zonal wave numbers and frequencies given by the sums and the differences of the corresponding "parent" wave numbers and frequencies. For example, at wintertime middle and high latitudes, a westward-propagating diurnal tide with zonal wavenumber 2 (DW2) is anticipated from the interaction of a stationary PW-1 with a migrating diurnal tide with zonal wavenumber one (DW1). Figure 14 adapted from Lieberman et al (2015) illustrates this process using hourly

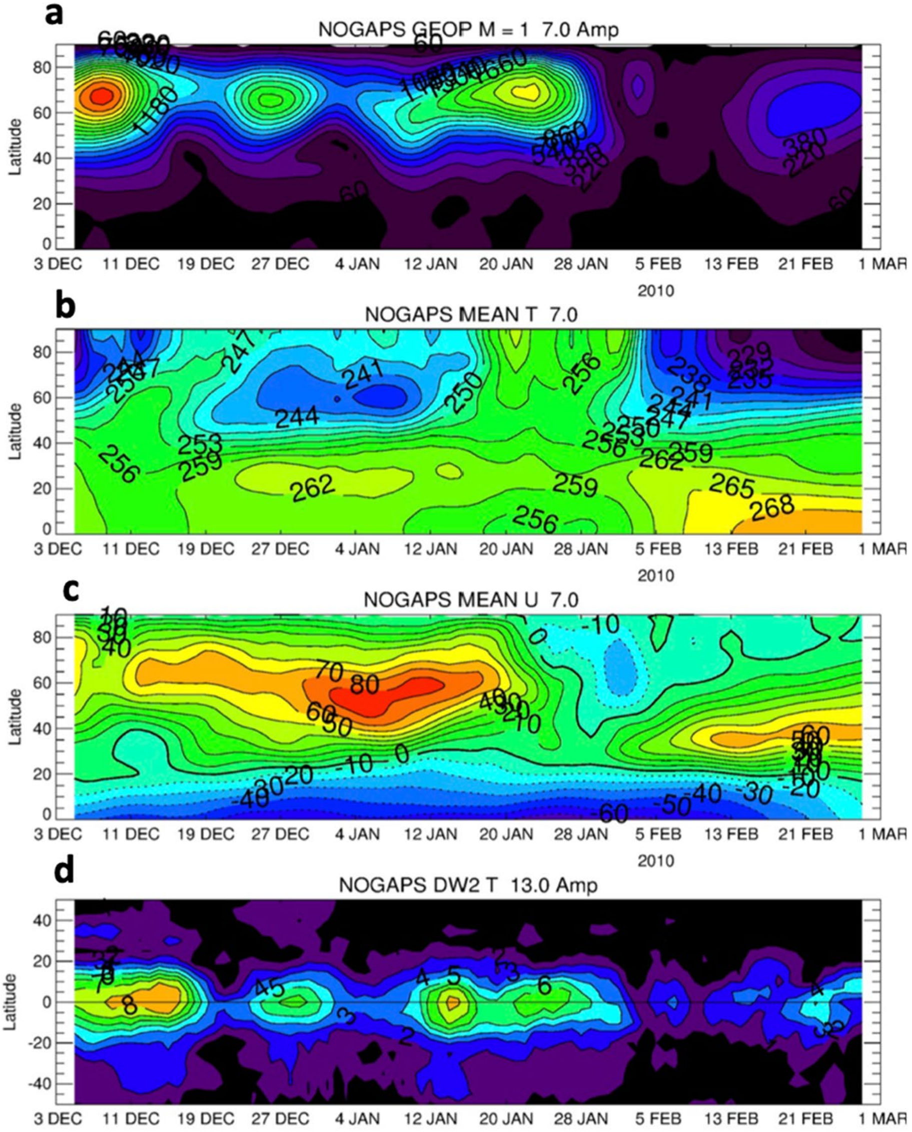

Fig. 14 Latitude–time plots of NOGAPS-ALPHA NH stratospheric PW-1 geopotential height amplitude (panel **a**), zonal mean temperature (panel **b**), zonal mean wind (panel **c**), and global mesospheric DW2 temperature amplitude (panel **d**) during December 2009–February 2010. The top three panels are near the stratopause (7 scale heights ≅ 49 km); the bottom panel is in the upper mesosphere (13 scale heights ≅ 91 km)

analyses from NOGAPS-ALPHA, a prototype vertical extension of the Navy's operational forecast model (Eckermann et al. 2009).

Figure 14 depicts the evolution, from December 2009 to February 2010, of northern hemisphere quasi-stationary PW-1 GPH amplitude (panel a), zonal mean temperature (panel b), and zonal mean wind (panel c) near the stratopause (7 scale heights ≅ 49 km), and global DW2 temperature amplitude (panel d) in the upper mesosphere (13 scale heights ≅ 91 km). PW-1 amplitudes are very strong at high northern latitudes in early December and late January, with a weaker maximum in late December. Following the PW-1 events in early December and late January, there is warming in the polar cap and weakening or reversal of the zonal jet. Despite DW2 temperature maximizing near the equator, its amplitude often appears to track the PW-1 amplitudes at high northern latitudes. Experiments with a mechanistic model confirmed that meridional advection of PW-1 zonal momentum by DW1 is the leading source of DW2. The study of Lieberman et al. (2015) indicates that PW–tide interaction imprints short-term variability associated with the wintertime polar stratosphere upon the global MLT.

8 F-region Variability

This section examines major SSW-driven variability in the upper thermosphere and ionosphere in COSMIC-2 and ionosonde observations. First, the SW2 near 300 km is derived from COSMIC-2 global ionospheric specification (GIS) during two recent major SSWs and the ionosondes provide observations of foF2 that support SEAs at high latitudes and at mid-latitudes. The GIS is a data assimilation system that provides electron densities on a three-dimensional global grid with a resolution of 5° longitude × 2.5° latitude × 20 km altitude, spanning from 120 to 700 km (Lin et al. 2017). It provides hourly global maps, which is critical for obtaining the daily amplitudes and phases of the tides using the Fourier transform. It is important to note that the daily Fourier fitting of hourly data does not allow for the separation of lunar (12.42 h) and solar (12.0 h) semidiurnal tides, so some contributions from the lunar tide cannot be excluded. The tides' relative amplitudes (with respect to the daily zonal mean) are used to minimize the effect of solar/geomagnetic activity. Since the data have been available since late 2019, we chose the major SSW events on 5 January 2021 and 16 February 2023. We focus on the SW2 as it is known to be strongly affected by SSWs (Pedatella et al. 2012).

Figure 15 (left) (a) shows the SW2 relative amplitude at 300 km as a function of latitude versus day from the 2021 SSW onset. Overplotted is the zonal wind at 10 hPa and 60°N (white contour). The red contour gives zonal winds at 1 hPa and 60°N. We observe clear enhancements in SW2 amplitudes during the 2021 SSW at EIA latitudes. Further, during the time period shown, SW2 enhancements occur whenever the zonal winds weaken. Panel (b) shows the SW2 relative amplitudes (blue) averaged around 15°N (5°N–20°N) from (a), along with the zonal winds from panel a (black and red). The correlation coefficient between zonal winds at 10 (1) hPa and SW2 amplitudes at 15°N and 300 km is − 0.59 (− 0.56). SW2 amplitudes in the EIA crest regions vary by a factor of 2, with smaller amplitudes when stratospheric winds are strong and enhancements when stratospheric winds are weak. The geomagnetic activity proxy Kp-index (blue) and the solar flux proxy F10.7 index (black) are shown in panel (c), indicating that these factors do not significantly affect the daily variability of the SW2.

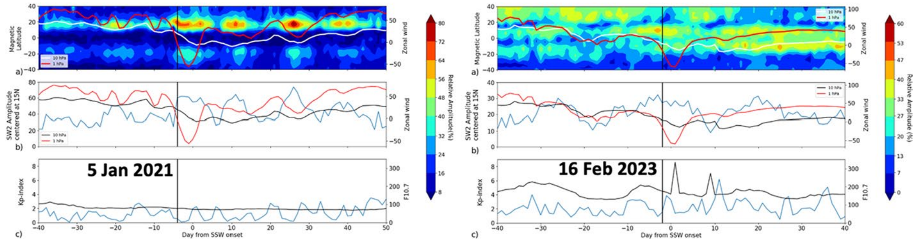

Fig. 15 (left, top panel) SW2 relative amplitude as a function of magnetic latitude and days from SSW onset at 300 km (averaged from 280–320 km), where day 0 is the SSW onset on 5 January 2021. Overplotted is the zonal wind at 60°N and 10 hPa (white) and 1 hPa (red). **(left, middle panel)** SW2 (blue) averaged around 15°N from (left, top panel) and the zonal wind at 10 hPa (black) and 1 hPa (red). **(left, bottom panel)** kp-index (blue) and F10.7 index (black). (right) as left panels but day 0 is 16 February 2023

The situation is different for 2023 (right panels), when the solar flux is higher than in 2021, and solar flares are present during the major SSW period. During the 2023 SSW, we do not see an apparent enhancement in the SW2 as in 2021, as the solar and geomagnetic activity is the primary reason for tidal variability. The correlation coefficient between zonal winds at 10 (1) hPa and SW2 amplitudes at 15°N and 300 km is -0.35 (-0.43) during this winter. Aggarwal et al. (2024) studied the response of the ionosphere to the strength of the polar vortex and the effect of solar/geomagnetic activity and showed similar masking of lower atmosphere forcing due to high solar flux.

Next, we look for signatures of vortex weakening in the ionosphere using ionosonde data. An ionosonde sends HF waves into the ionosphere and performs a frequency sweeping in the 1–30 MHz range. Each wave sent by the ionosonde is reflected when its frequency becomes equal to the local plasma frequency of the ionized medium, allowing an electron density profile reconstruction of the low-altitude ionosphere. The foF2 frequency corresponds to the maximum frequency reached by the ionosonde and is proportional to the maximum electron density observed at the peak of the F2 layer, the highest and densest layer of the ionosphere (see Reinish and Galkin 2011 and references therein). Its altitude is between 250 and 400 km and depends on local conditions (solar illumination and particle precipitation). The altitude of foF2, called (hmF2), obtained from an ionosonde is a virtual height as it corresponds to the time it takes for the wave to travel to the ionosphere and return to the ground. However, the speed of light is assumed in this calculation, whereas the wave undergoes breaking in the ionospheric medium, so that the real height of the echoes is lower than the virtual height. Finally, it is possible to obtain an estimation of the Total Electron Content (TEC) from the electron density values derived from an ionosonde, but it corresponds only to the density integration up to the F2-peak.

Ionosonde observations of foF2 (250–400 km) were used to construct 40-day SEA at 8 ionosonde stations, spread over four longitude sectors at both high and mid-latitudes (see Table 2). Ionosondes used in this study are from the GIRO network (Reinisch and Galkin 2011). We removed all points with moderate to active magnetic and solar activity (Ap ≥ 10 nT and F10.7 ≥ 80 sfu). Given the periods of operation of these ionosondes and with such activity criteria, only a reduced number of events are retained in the SEA (maximum of 5 events: 2006, 2009, 2010, 2018, 2019) centered around the onset of wind reversals at 1 hPa followed by ESs. Some ionosondes did not operate for some of these events and have only 3 or 4 events included in the SEA. Finally, even for the considered events, some data points may have been removed if magnetic or solar activity became too high.

Table 2 Location of 8 ionosondes used in the SEA

	Western North America	Eastern North America	Europe	Aisa
High latitude	GAK 62.3°N, 145.3°W	SON 67°N, 51°W	TRO 69.7°N, 19°E	NOR 69.2°N, 88°E
Mid latitude	PTA 34.6°N, 120.7°W	MIL 42.6°N, 71.5°W	ROM 41.9°N, 12.5°E	JEJ 33.4°N, 126.3°E

GAK = Gakona Alaska USA, SON = Sondrestorm Greenland, TRO = Tromso Norway, NOR = Norilsk Russia, PTA = Point Arguello California USA, MIL = Millstone Hill Massachusetts USA, RM = Rome, Italy, and JEJ = Jeju South Korea

Figure 16 shows the SEA median of foF2. Results show slight increases after day 0, during the hours around local noon for all high-latitude stations and for Point Arguello and Rome at mid-latitudes. Note, local noon varies in UT given on the y-axis. The increases

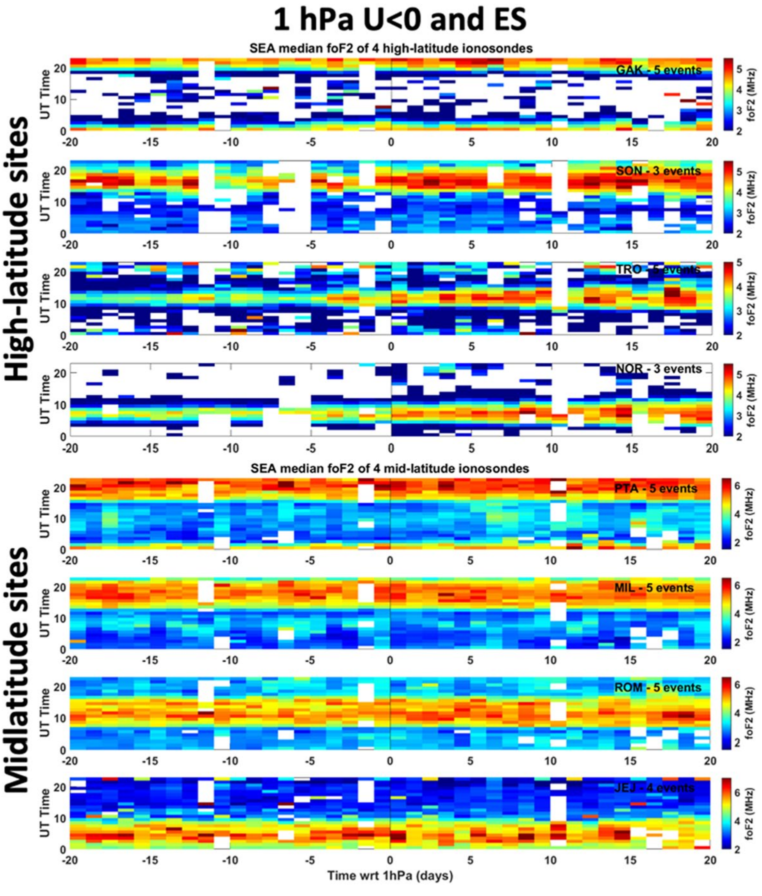

Fig. 16 SEAs as a function of day and universal time of foF2 at (top) 4 high-latitude ionosonde stations and (bottom) 4 mid-latitude ionosonde stations with day 0 for events when 1 hPa winds reversed followed by an ES and there are quiet solar (f10.7 < = 80) and geomagnetic conditions (Ap < = 10)

after day 0 are slightly more pronounced at high latitudes. The % change in foF2 at noon from before the SSW (over 12 days) to after the SSW (over 12 days) is 5–17% at high-latitude stations and 2–6% at mid-latitude stations. The % change in TEC (not shown) at noon from before to after day 0 is: 10–35% at high-latitude stations and 3–15% at mid-latitude stations. A slight enhanced variability in foF2 and TEC as seen as an increase in interquartile range of the SEA (not shown). On the contrary, no clear change in virtual height (hmF2) is observed (not shown).

These results show that the midday ionosphere, and in particular its F2-layer, exhibits slight increases in density and more variability after the 1 hPa wind reversal. More surprising, these effects seem to last for many days. Overall, the spread in noontime changes in foF2 and TEC among individual events remains relatively limited because the seasonal and quiet magnetospheric conditions are relatively similar. However, the number of events is limited and there are data gaps when conditions $Ap < 10$ nT or $F107 < 80$ sfu are not met. Thus, caution must be used in the interpretation of these results due to the small sample size and because ionosonde data are often difficult to interpret, due, for example, to complex propagation effects. In addition, as most stratopause warming events followed by ESs occurred in January, separation of stratopause warming-induced subseasonal effects from the effects of seasonal increases in foF2 (and TEC) from January to February (Goncharenko et al. 2018) presents an additional challenge. Nevertheless, these results call for further investigation, since they suggest that an increase in electron density is observed after vortex weakening events, although with generally clearer signatures at mid-latitudes (Mošna et al. 2021; Goncharenko et al. 2021b).

9 Future aspects: How will the polar vortex change?

Enhanced CO_2 concentrations lead to cooling of the middle atmosphere. The reason is that the cooling to space from CO_2 mainly balances solar, chemical and dynamical heating rates in the middle atmosphere (Manabe 1967; Randel et al. 2009; Santer et al. 2023). Moreover, ozone experienced a dramatic decrease in the latter half of the twentieth century due to the emissions of ozone-depleting substances (i.e., chlorofluorocarbons, CFCs). This long-term variability of the polar ozone content contributes to the strength of the polar vortex. It has been shown that the Antarctic ozone hole accelerated the southern polar vortex jet (Gillett & Thompson 2003). Stratospheric ozone levels are now slowly recovering after the Montreal Protocol banned the use of CFCs. This will lead to overall warming in the polar stratosphere, but which will not overcome the cooling due to CO_2 and other greenhouse gases (Kirner et al. 2015). Furthermore, a cooler stratosphere slows down the chemical reactions which destroy ozone, leading to further increases in stratospheric ozone.

These changes in stratospheric temperatures and ozone content in the future also lead to dynamical changes (Langematz et al. 2003). Climate models predict that the global mean residual circulation will accelerate in the future, leading to enhanced transport to polar latitudes especially in the Northern Hemisphere and enhanced descent in the polar winter middle atmosphere (see review by Butchart 2014). Since this circulation is linked to polar vortex dynamics, this suggests that the polar vortex may weaken in the future. Arctic sea-ice loss might also impact strength of the polar vortex via changes in the upward propagation of waves (Liang et al. 2024).

While a weaker future Arctic polar vortex implies more disturbances and increased frequency of SSWs, no robust evidence of future changes in major SSWs has been obtained from chemistry climate models (Ayarzaguena et al. 2018). Dimdore-Miles et al. (2021) modeled changes in SSW frequency over 1000-year pre-industrial simulation and showed that SSWs experience multidecadal variability in periods of 60 to 90 years, which is associated with long-term variability in the amplitude of the quasi-biennial oscillation (QBO). In the southern hemisphere, SSWs are rare and only a few major or minor SSWs have been observed. This is due to the strong and stable southern polar vortex and weak PW activity in the absence of land–sea contrasts. It has been shown that in the future the probability of major SSWs in the southern hemisphere is expected to diminish even further as the polar vortex is expected to strengthen as CO_2 concentrations increase (Jucker et al. 2021).

Related to the expected dynamical changes in the southern hemispheric polar atmosphere, Maliniemi et al. (2020) investigated the polar NO_x distribution during the twenty-first century using simulations of a free-running version of the chemistry climate model WACCM6 driven by four different future scenarios. The results reveal that energetic particle precipitation (EPP)-produced NO_x in the Antarctic upper atmosphere descends faster to stratospheric altitudes during the winter in the stronger greenhouse gas scenarios by the end of the twenty-first century. The enhanced transport is caused by an accelerated residual circulation in the Antarctic mesosphere due to climate change. Thus, the EPP-related atmospheric effects are expected to become larger in a warmer climate, regardless of the level of EPP activity. Moreover, several studies show that the reduction in anthropogenic ozone-depleting substances fortifies the role of the natural EPP-related chemical impact on stratospheric ozone. Maliniemi et al. (2021) show how the enhanced stratospheric NO_x leads to more seasonal ozone depletion in the Coupled Model Intercomparison Project Phase 6 scenarios. Recovery to 1960s CFC levels is estimated to occur sometime after 2050. As stated above, a cooler stratosphere slows down the chemical reactions which destroy ozone. This will cause a net positive ozone production in stronger greenhouse gas emission scenarios and will lead to a super recovery of ozone. The model simulations, however, show that the enhanced descent of EPP-NO_x may counteract this effect and can potentially prevent a super recovery of ozone in the Antarctic upper stratosphere. Note the fidelity of climate models with parameterized GWs in the polar winter mesopause region, especially in the southern hemisphere, can be low (e.g., Harvey et al. 2022a).

Earlier works of Funke et al. (2014) have pointed out a potential complex interplay, where NO_x interferes with ozone loss driven by the halogen species ClO and BrO. This was observationally confirmed by Gordon et al. (2021) who found a positive correlation between EPP and $ClONO_2$ in the upper stratosphere in the early spring and in the lower stratosphere in late spring. Similarly, Maliniemi et al. (2022) apply the chemistry climate model SOlar Climate Ozone Links (SOCOL) linked to the Max-Planck-Institute for Meteorology Ocean Model (MPIOM) to the CFC era and show that EPP has been a significant modulator of reactive chlorine in the Antarctic stratosphere, thus impacting ozone depletion by CFC emissions and modulating the magnitude of the Antarctic ozone hole. Both the results of Gordon et al. (2021) and Maliniemi et al. (2022) confirm that stratospheric chlorine has acted as a buffer for ozone depletion by EPP via limiting the NO_x and HO_x catalytic cycle efficiencies. With the Montreal Protocol and the declining levels of CFC chemicals, we can expect more efficient chemical ozone depletion by EPP in the future. The stratospheric ozone levels and the associated impact on polar vortex strength are therefore likely to be more dependent on solar cycle EPP impacts in the future.

10 Conclusions

As part of the ISSI special issue on “Physical links between Weather and Climate in Space and the Lower Atmosphere,” this paper summarizes known temperature, neutral wind, composition, PW, GW, and tidal signatures in the MLT during weak polar vortex events. In this work, we performed SEAs centered on major SSW onsets as well as the onset of “stratopause warmings” followed by ES events. The motive for both SEAs was to test the sensitivity of disturbance altitude in the prediction of upper atmosphere variability. Indeed, both observational and modeling results suggest zonal wind and SW2 responses in the MLT are larger when SEAs use central dates at 1 hPa vs. 10 hPa. Alternatively, the SSW-related variability in the non-migrating DW2 tide is best predicted by PW-1 amplitudes in the upper stratosphere rather than zonal mean zonal wind reversals at 10 hPa or at 1 hPa. For every dynamical and chemical diagnostic examined here, event-to-event variability is large in both SEAs. Thus, conclusions drawn based on any one event are less robust than those based on many events.

Results shown here reveal signatures of vortex weakening in a variety of diagnostics and using different observational platforms and numerical simulations. A summary of key points is:

- SEAs of 87 km temperature at Svalbard display large variability (up to ~ 20 K) within individual warming events as well as event-to-event. This large variability is attributed to the dynamically active conditions in the Arctic polar winter upper mesosphere. In both SEAs, nearly all events show a gradual warming of 20–30 K in the 20-day period after the onset that is likely due to enhanced GW-driven descent.
- SEAs of 87 km temperature at five locations from Catania, Italy, to Alomar, Norway (38–69°N), show ~ 30 K warming at high latitudes in the 20 days after onset and ~ 10 K cooling at mid-latitude sites in the 40 days following onset. This mid-latitude cooling is consistent with the known out-of-phase SSW-induced temperature anomalies in low-to-mid-latitudes compared to high latitudes, driven by an anomalous meridional circulation cell (e.g., Miyoshi et al. 2015). However, some of this cooling trend may be seasonal variability, especially for years with mid-February SSWs (2010, 2018, 2023).
- SEAs of MLS polar cap average temperature in the MLT are consistent with the airglow spectrometer results. A notable difference between the major SSW SEA and the stratopause warming SEA is the maximum stratospheric warming and mesospheric cooling occur in the week prior to SSW onset and in the week following stratopause warming onset.
- SEAs of SABER polar cap averaged O_3, O, H, and T anomalies near 92 km reveal large event-to-event variability during stratopause warmings followed by ES events. Despite this, signatures of descent following the warming are common. In fact, ES-induced O_3 decreases and H increases are very long-lasting and do not return to pre-SSW values even after 60 days, suggesting a seasonal contribution.
- SEAs of MIPAS CH_4, CO, NO_y in the stratosphere and mesosphere reveal large event-to-event variability in the magnitude and timing of anomalies. Temperature variability shows stratospheric warming/mesospheric cooling, as expected. Tracer variability shows stratospheric mixing near onset and mesospheric descent in the two months following onset.
- SEA means of O_3 and H_2O anomalies in the SMLT at Ny-Alesund (79°N) show high ozone and water vapor are transported from mid-latitudes to polar latitudes by PWs

around day 0 and that these increases persist for weeks to a month or more (for ozone). Water vapor decreases from days + 10 to + 50 are due to descent of dry air from the upper mesosphere.

- Analysis of GW forcing in SD-WACCMX during the 2024 SSW shows a more gradual evolution of mesospheric temperature in the high-resolution simulation compared to coarse resolution. After the SSW, the upper mesosphere is warmer in the high-resolution run, consistent with enhanced descent.
- SEA means of MLS derived winds and PW variations indicate 1) MLT wind reversals occur 5-days prior to major SSW onset, whereas the stratopause warming SEA shows the onset of easterlies simultaneously from 30 to 95 km, 2) PWs maximize 3 (1) weeks prior to onset in the major SSWs (stratopause warmings). Note large event-to-event variations are embedded in SEA means.
- SEAs in SuperDARN reveal westward and poleward wind shifts in the MLT a few days after stratopause warming onset; however, the timing with respect to day 0 varies event-to-event. There are enhanced Q6DW amplitudes in the 2-weeks after day 0 though, again, there is considerable event-to-event variability in terms of the amplitude and timing of the enhancement. Finally, while SW2 enhancements "cluster" around day + 13 for individual events, there is significant event-to-event variability in the SW2 response. Results suggest zonal winds and the SW2 in the MLT are more sensitive to changing propagation conditions in the upper stratosphere rather than at 10 hPa.
- Stratopause warming SEAs of SW2 in meteor radar and SABER observations reveal enhancements in the month after onset.
- SEAs in WACCMX upper mesospheric zonal wind show a slight decrease prior to day 0 and an enhancement after day + 10, consistent with observations. There are weak (1–1.5 K or 15–20%) decreases in DW1 around day 0 and SW2 enhancements of ~ 20–30 m/s peak from day + 7 to day + 10. There is a second SW2 enhancement from day + 20 to day + 25 that was also observed by SuperDARN that warrants further study. Both U and SW2 responses are larger when SEAs are organized with respect to onset dates of wind reversals at 1 hPa compared to 10 hPa.
- Analysis of SW2 zonal wind amplitude in UA-ICON during the 2023 SSW is consistent with WACCMX and SuperDARN and shows enhanced amplitudes on day + 8.
- Analysis of DW2 temperature amplitude in NOGAPS-ALPHA during the 2010 SSW shows DW2 amplitude at the Equator tracks PW-1 amplitudes at high latitudes due to PW-tide interactions.
- In the F-region, analysis of COSMIC-2 GIS data reveals SW2 enhancements at 300 km at EIA latitudes during the 2021 SSW. Moreover, SW2 amplitudes at this latitude and altitude grow whenever stratospheric winds weaken ($r = -0.56$ with winds at 10 hPa, $r = -0.59$ with winds at 1 hPa). When solar flux is high, as it is in 2023, SSW-induced enhancements to SW2 are masked in the F-region.
- SEAs in ionosondes show increases in foF2 at high latitudes at local noon following 1 hPa wind reversals and these increases persist for many days. However, caution should be used interpreting these results due to the small number of events analyzed, complex propagation effects, and the potential contribution of seasonal variations.
- The paper ends with a discussion on how the strength of the polar vortex and the frequency of SSWs might change in the future. Predictions of vortex strength are impacted by multiple competing processes: Increases in greenhouse gases are expected to strengthen the vortex, ozone recovery in the Antarctic is expected to weaken the vortex, and changes in radiation, dynamics, and chemistry must also be considered. Climate models predict an acceleration of the residual circulation, potentially weakening the

polar vortex due to enhanced descent and adiabatic warming. Arctic sea ice loss may also influence residual circulation and thereby vortex strength by altering wave propagation. While a weaker polar vortex could be associated with increased SSW frequency in the Northern Hemisphere, models do not provide robust scenarios of future changes. Higher-resolution models with improved treatment of GWs, tides, and other physical processes are required for more accurate cause-and-effect assessments.

Acknowledgements This paper is an outcome of the Workshop “Physical Links Between Weather and climate in Space and the Lower Atmosphere” held at the International Space Science Institute (ISSI) in Bern, Switzerland (22–26 January 2024). The coauthors thank ISSI for hosting the workshop and for providing accommodations in Bern to attend the workshop. VLH thanks Prof. Claudia Stolle for the invitation to participate in this ISSI workshop. VLH was supported by NASA grants 80NSSC23K0848, 80NSSC22K0017, 80NSSC22K1074, 80NSSC24K0269 and NSF grant AGS2411429. DA acknowledges NASA grant 80NSSC22K1010. BF acknowledges financial support from the Agencia Estatal de Investigación (grant no. PID2022-141216NB-I00/AEI/10.13039/501100011033) and the Severo Ochoa grant CEX2021-001131-S funded by MCIN/AEI/10.13039/501100011033. EB was supported by NSF grant 2329957. HLL acknowledges partial support by NASA Grants 80GSFC18C0007. NP acknowledges support from NASA grants 80NSSC23K0418 and NNH220B82A. WvC was supported by NSF AGS 1341885. This material is based, in part, upon work supported by the National Center for Atmospheric Research, which is a major facility sponsored by the U.S. National Science Foundation under Cooperative Agreement 1852977. High-end computing resources were provided by NASA to run WACCMX on the Pleiades supercomputer at the NASA Ames research center. The GRIPS instruments at the sites ALR, UFS, WUP, OHP, CAT, and ABA were at least in parts deployed and operated within different projects funded by the European Union, the Federal Ministry of Education and Research of Germany, and the Bavarian Ministry for the Environment and Consumer Protection. The authors thank the Svalbard spectrometer PI Fred Sigernes for instrument maintenance and the data. Gunter Stober and Guochun Shi are members of the Oeschger Center for Climate Change Research and are supported by the Swiss National Science Foundation (grant no. 200021-200517/1). The radiometers of the University Bern deployed at Ny-Alesund are supported through AWIPEV under grant AWIPEV_0023. Meteor radar winds and related research were supported by ISSI in Bern through ISSI International Team project #23-580 "Meteors and phenomena at the boundary between Earth’s atmosphere and outer space." Gunter Stober acknowledges the support of the meteor radar observations by Njal Gulbrandsen, Masaki Tsutsumi, and Christoph Jacobi. The authors have no competing interests to declare that are relevant to the content of this article. All authors certify that they have no affiliations with or involvement in any organization or entity with any financial interest or non-financial interest in the subject matter or materials discussed in this manuscript. The authors have no financial or proprietary interests in any material discussed in this article.

MLS v5.1 data are available from the NASA Goddard Space Flight Center for Earth Sciences Data and Information Services Center (DISC) at https://mls.jpl.nasa.gov/. MERRA-2 data are available at MDISC, managed by the NASA Goddard Earth Sciences (GES) DISC at https://gmao.gsfc.nasa.gov/reanalysis/. The MIPAS data can be obtained from the KITopen repository (see https://doi.org/10.5445/IR/1000156457, Funke et al., 2023 [dataset]). SABER data are available at http://saber.gats-inc.com/data.php. SuperDARN data are available from Virginia Tech at vt.superdarn.org. The hourly SuperDARN meteor echo winds are available from Chartier & Wiker (2023). COSMIC-2 GIS data are publicly available at http://formosat7.earth.ncku.edu.tw. Conversion into geomagnetic coordinates was performed using the Python wrapper for the Apex fortran library that can be downloaded from https://doi.org/10.5281/zenodo.1214206. The daily averaged F10.7 cm radio flux is from NASA/GSFC OMNIWeb at https://omniweb.gsfc.nasa.gov/form/dx1.html. Svalbard spectrometer data are available on request by contacting the instrument PI F. Sigernes (freds@unis.no). The GROMOS-C and MIAWARA-C level-2 data are provided by the Network for the Detection of Atmospheric Composition Change (NDACC) and are available at the NDACC data repository https://www-air.larc.nasa.gov/pub/NDACC/PUBLIC/meta/mwave/. WACCMX is part of the Community Earth System Model (CESM), and the source code is available at https://github.com/ESCOMP/CESM. The SD-WACCMX simulation output is available via https://doi.org/10.26024/5b58-nc53. The ICON model is open source available at https://doi.org/10.35089/WDCC/IconRelease2024.10.

Author Contributions VLH wrote the abstract, introduction, and conclusions, and generated Figs. 3 and 8 and associated text. She also edited text provided by the coauthors. Coauthors are listed in alphabetical order. Coauthor contributions are as follows: Noora Partamies (Fig. 1), Sabine Wüst, Carsten Schmidt, and Michael Bittner (Fig. 2), Jia Jia (Fig. 4), Bernd Funke (Fig. 5), Gunter Stober and Guochun Shi (Figs. 6

and 10), Hanli Liu (Fig. 7), Wim van Caspel (Fig. 9), Yosuke Yamazaki (Fig. 11), Nick Pedatella (Fig. 12), Claudia Stephan and Yosuke Yamazaki (Fig. 13), Ruth Lieberman (Fig. 14), Deepali Aggarwal (Fig. 15), and Aurélie Marchaudon (Fig. 16 and Table 2). Ville Maliniemi and Hilde Nesse wrote Sect. 9. Erich Becker and Larisa Goncharenko provided valuable feedback on the text.

References

Aa E, Pedatella NM, Liu G (2024) Impacts of the sudden stratospheric warming on equatorial plasma bubbles: suppression of EPBs and Quasi-6-Day oscillations. Remote Sensing 16(8):1469. https://doi.org/10.3390/rs16081469

Aggarwal D, Oberheide J, Pedatella NM, Martinez BC (2024) The semidiurnal tidal response of the low latitude ionosphere to the strength of the polar vortex from COSMIC-2 global ionospheric specification. Geophys Res Lett. https://doi.org/10.1029/2024GL111313

Andrews DG (1985) Wave–mean–flow interaction in the middle atmosphere. Adv Geophys A 28:249–275. https://doi.org/10.1016/S0065-2687(08)60226-5

Ayarzaguena B et al (2018) No robust evidence of future changes in major stratospheric sudden warmings: a multi-model assessment from CCMI. Atmos Chem Phys 18:11277–11287. https://doi.org/10.5194/acp-18-11277-2018

Baldwin MP, Dunkerton TJ (2001) Stratospheric harbingers of anomalous weather regimes. Science 294:581–584. https://doi.org/10.1126/science.1063315

Baldwin MP, Ayarzagüena B, Birner T, Butchart N, Butler AH, Charlton-Perez AJ et al (2021) Sudden stratospheric warmings. Rev Geophys 59:e2020RG000708. https://doi.org/10.1029/2020RG000708

Becker E, Vadas SL (2018) Secondary gravity waves in the winter mesosphere: results from a high-resolution global circulation model. JGR Atmos 123:2605–2627. https://doi.org/10.1002/2017JD027460

Becker E, Goncharenko L, Harvey VL, Vadas SL (2022a) Multi-step vertical coupling during the January 2017 sudden stratospheric warming. J Geophys Res Space Phys 127:e2022JA030866. https://doi.org/10.1029/2022JA030866

Becker E, Vadas SL, Bossert K, Harvey VL, Zülicke C (2022b) A high-resolution whole-atmosphere model with resolved gravity waves and specified large-scale dynamics in the troposphere and stratosphere. J Geophys Res Atmos 127:e2021JD035018. https://doi.org/10.1029/2021JD035018

Borchert S, Zhou G, Baldauf M, Schmidt H, Zängl G, Reinert D (2019) The upper-atmosphere extension of the ICON general circulation model (version: ua-icon-1.0). Geosci Model Dev. https://doi.org/10.5194/gmd-12-3541-2019

Bosilovich M, Akella S, Coy L, Cullather R, Draper C, Gelaro R et al (2015) MERRA-2: initial evaluation of the climate, NASA Tech. Rep. Series on Global Modeling and Data Assimilation, NASA/TM–2015-104606 (vol 43)

Brasseur GP, Solomon S (2005) Aeronomy of the middle atmosphere, 3rd edn. Springer, Dordrecht

Butchart N (2014) The Brewer–Dobson circulation. Rev Geophys 52:157–184. https://doi.org/10.1002/2013RG000448

Butler AH et al (2015) Defining sudden stratospheric warmings. Bull Am Meteorol Soc 96:1913–1928. https://doi.org/10.1175/BAMS-D-13-00173.1

Butler A, Sjoberg JP, Seidel DJ, Rosenlof KH (2017) A sudden stratospheric warming compendium. Earth Syst Sci Data 9(1):63–76. https://doi.org/10.5194/essd-9-63-2017

Chandran A, Collins RL, Garcia RR, Marsh DR (2011) A case study of an elevated stratopause generated in the whole atmosphere community climate model. Geophys Res Lett 38:L08804. https://doi.org/10.1029/2010GL046566

Chartier AT, Wiker JR (2023) SuperDARN meteor winds product (1993–2023) (version 2). Zenodo. https://doi.org/10.5281/zenodo.8193784

Chisham G, Freeman MP (2013) A reassessment of SuperDARN meteor echoes from the upper mesosphere and lower thermosphere. J Atmos Solar Terr Phys 102:207–221. https://doi.org/10.1016/j.jastp.2013.05.018

Chau JL, Goncharenko LP, Fejer BG, Liu H-L (2012) Equatorial and low latitude ionospheric effects during sudden stratospheric warming events. Space Sci Rev 168:385–417. https://doi.org/10.1007/s11214-011-9797-5

Cho Y-M, Shepherd GG, Won Y-I, Sargoytchev S, Brown S, Solheim B (2004) MLT cooling during stratospheric warming events. Geophys Res Lett. https://doi.org/10.1029/2004GL019552

de Wit RJ, Hibbins RE, Espy PJ (2015) The seasonal cycle of gravity wave momentum flux and forcing in the high latitude northern hemisphere mesopause region. JASTP 127:21–29. https://doi.org/10.1016/j.jastp.2014.10.002

Dimdore-Miles O, Gray L, Osprey S (2021) Origins of multi-decadal variability in sudden stratospheric warmings. Weather Clim Dynam 2:205–231. https://doi.org/10.5194/wcd-2-205-2021

Dowdy AJ, Vincent RA, Tsutsumi M, Igarashi K, Murayama Y, Singer W, Murphy DJ, Riggin DM (2007) Polar mesosphere and lower thermosphere dynamics: 2. Response to sudden stratospheric warmings. J Geophys Res 112:D17105. https://doi.org/10.1029/2006JD008127

Duck TJ, Whiteway JA, Carswell AI (1998) Lidar observations of gravity wave activity and Arctic stratospheric vortex core warming. Geophys Res Lett 25(15):2813–2816. https://doi.org/10.1029/98GL02113

Duck TJ, Whiteway JA, Carswell AI (2001) The gravity wave-arctic stratospheric vortex interaction. J Atmos Sci 58(23):3581–3596. https://doi.org/10.1175/1520-0469(2001)058%3c3581:TGWASV%3e2.0.CO;2

Dyrland ME, Mulligan FJ, Hall CM, Sigernes F, Tsutsumi M, Deehr CS (2010) Response of OH airglow temperatures to neutral air dynamics at 78°N, 16°E during the anomalous 2003–2004 winter. J Geophys Res 115(D7):D07103. https://doi.org/10.1029/2009JD012726

Eckermann SD, Hoppel KW, Coy L, McCormack JP, Siskind DE, Nielsen K, Kochenash A, Stevens MH, Englert CR, Hervig M (2009) High-altitude data assimilation system experiments for the northern summer mesosphere season of 2007. J Atmos Solar Terr Phys 71:531–551. https://doi.org/10.1016/j.jastp.2008.09.036

Enengl F, Partamies N, Ivchenko N, Baddeley L (2021) On the relationship of energetic particle precipitation and mesopause temperature. Ann Geophys 39:795–809. https://doi.org/10.5194/angeo-39-795-2021

Ern M, Preusse P, Gille JC, Hepplewhite CL, Mlynczak MG, Russell JM III, Riese M (2011) Implications for atmospheric dynamics derived from global observations of gravity wave momentum flux in stratosphere and mesosphere. J Geophys Res 116:D19107. https://doi.org/10.1029/2011JD015821

Esplin R, Mlynczak MG, Russell J, Gordley L, & Team, S. (2023) Sounding of the atmosphere using broadband emission radiometry (SABER): instrument and science measurement description. Earth Space Sci 10(9):e2023EA002999. https://doi.org/10.1029/2023EA002999

Fang TW, Fuller-Rowell T, Wang H, Akmaev R, Wu F (2014) Ionospheric response to sudden stratospheric warming events at low and high solar activity. J Geophys Res Space Phys 119(9):7858–7869. https://doi.org/10.1002/2014JA020142

Fang TW, Fuller-Rowell T, Yudin V, Matsuo T, Viereck R (2018) Quantifying the sources of ionosphere day-to-day variability. J Geophys Res Space Phys 123(11):9682–9696. https://doi.org/10.1029/2018JA025525

Forbes JM (1995) Tidal and planetary waves, in The Upper Mesosphere and lower thermosphere: a review of experiment and theory. Geophys Monogr Ser 87. In: Johnson RM, Killeen TL (eds), AGU, Washington, DC, pp 67–87. https://doi.org/10.1029/GM087p0067

Forbes JM, Zhang X, Palo S, Russell J, Mertens CJ, Mlynczak M (2008) Tidal variability in the ionospheric dynamo region. J Geophys Res Space Phys. https://doi.org/10.1029/2007JA012737

Frissell NA, Baker JBH, Ruohoniemi JM, Greenwald RA, Gerrard AJ, Miller ES, West ML (2016) Sources and characteristics of medium-scale traveling ionospheric disturbances observed by high-frequency radars in the North American sector. J Geophys Res Space Phys 121(4):3722–3739. https://doi.org/10.1002/2015JA022168

Fritts DC, Nastrom GD (1992) Sources of mesoscale variability of gravity waves. Part II: Frontal, convective, and jet stream excitation. J Atmos Sci 49(2):111–127.

Froidevaux L, Read WG, Jiang YB, Jimenez C, Filipiak MJ, Schwartz MJ et al (2006) Early validation analyses of atmospheric profiles from EOS MLS on the Aura satellite. IEEE Trans Geosci Remote Sens 44(5):1106–1121. https://doi.org/10.1109/TGRS.2006.864366

Funke B, López-Puertas M, Stiller GP, von Clarmann T (2014) Mesospheric and stratospheric NO_y produced by energetic particle precipitation during 2002–2012. J Geophys Res Atmos 119:4429–4446. https://doi.org/10.1002/2013JD021404

Funke B et al (2023a) Michelson interferometer for passive atmospheric sounding institute of meteorology and climate research/Instituto de Astrofísica de Andalucía version 8 retrieval of nitric oxide and lower-thermospheric temperature. Atmos Meas Tech 16:2167–2196. https://doi.org/10.5194/amt-16-2167-2023

Funke B, von Clarmann T, García-Comas M, Glatthor N, Grabowski U, Höpfner M, Kellmann, Kiefer MS, Laeng A, Linden A, López-Puertas M, Stiller GP (2023) MIPAS IMK/IAA version 8 retrieval of nitric oxide and lower thermospheric temperature, KITopen. https://doi.org/10.5445/IR/1000156457

Gelaro R et al (2017) The modern-era retrospective analysis for research and applications, version 2 (MERRA-2). J Climate 30:5419–5454. https://doi.org/10.1175/JCLI-D-16-0758.1

Gillett NP, Thompson DWJ (2003) Simulation of recent Southern Hemisphere climate change. Science. https://doi.org/10.1126/science.1087440

Glatthor N et al (2024) IMK–IAA MIPAS retrieval version 8: CH_4 and N_2O. Atmos Meas Tech 17:2849–2871. https://doi.org/10.5194/amt-17-2849-2024

Goncharenko LP, Coster AJ, Chau JL, Valladares CE (2010) Impact of sudden stratospheric warmings on equatorial ionization anomaly. J Geophys Res 115:A00G07. https://doi.org/10.1029/2010JA015400

Goncharenko L, Chau JL, Condor P, Coster A, Benkevitch L (2013) Ionospheric effects of sudden stratospheric warming during moderate-to-high solar activity: case study of January 2013. Geophys Res Lett 40(19):4982–4986. https://doi.org/10.1002/grl.50980

Goncharenko LP, Coster AJ, Zhang S-R, Erickson PJ, Benkevitch L, Aponte N et al (2018) Deep ionospheric hole created by sudden stratospheric warming in the nighttime ionosphere. J Geophys Res Space Physics 123:7621–7633. https://doi.org/10.1029/2018JA025541

Goncharenko LP, Harvey VL, Liu H, Pedatella NM (2021a) Sudden stratospheric warming impacts on the ionosphere-thermosphere system—A review of recent progress. In: Huang C, Lu G (eds), Zhang Y, Paxton L (eds. In Chief) Space physics and Aeronomy, Volume 5, space weather effects and applications. Geophysical Monograph Series, pp 369–400. https://doi.org/10.1002/9781119815617.ch16

Goncharenko LP, Harvey VL, Greer KR, Zhang S-R, Coster AJ, Paxton LJ (2021b) Impact of September 2019 Antarctic sudden stratospheric warming on mid-latitude ionosphere and thermosphere over North America and Europe. Geophys Res Lett 48:e2021GL094517. https://doi.org/10.1029/2021GL094517

Gordon EM, Seppälä A, Funke B, Tamminen J, Walker KA (2021) Observational evidence of energetic particle precipitation NO_x (EPP-NO_x) interaction with chlorine curbing Antarctic ozone loss. Atmos Chem Phys 21:2819–2836. https://doi.org/10.5194/acp-21-2819-2021

Hagan ME, Roble RG (2001) Modeling diurnal tidal variability with the National Center for Atmospheric Research thermosphere-ionosphere-mesosphere-electrodynamics general circulation model. J Geophys Res 106:24869–24882. https://doi.org/10.1029/2001JA000057

Hall C, Tsutsumi M (2020) Neutral temperatures at 90 km altitude over Svalbard (78° N 16° E), 2002–2019, derived from meteor radar observations. Polar Sci 24:100530. https://doi.org/10.1016/j.polar.2020.100530

Hall CM, Tsutsumi M (2013) Changes in mesospheric dynamics at 78° N, 16° E and 70° N, 19° E: 2001–2012. J Geophys Res Atmos 118:2689–2701. https://doi.org/10.1002/jgrd.50268

Harvey VL, Randall CE, Goncharenko L, Becker E, France J (2018) On the upward extension of the polar vortices into the mesosphere. J Geophys Res Atmos 123:9171–9191. https://doi.org/10.1029/2018JD028815

Harvey VL, Pedatella NM, Becker E, Randall CE (2022a) Evaluation of polar winter mesopause wind in WACCMX+DART. J Geophys Res Atmos. https://doi.org/10.1029/2022JD037063

Harvey VL et al (2022b) Improving ionospheric predictability requires accurate simulation of the mesospheric polar vortex, perspective. Front Astron Space Sci Space Physics 9:1041426. https://doi.org/10.3389/fspas.2022.1041426

Harvey VL, Randall CE, Goncharenko L, Becker E, Forbes J, Carstens J, Xu S, France J, Zhang S-R, Bailey S (2023) CIPS observations of gravity wave activity at the edge of the polar vortices and coupling to the ionosphere. J Geophys Res Atmos. https://doi.org/10.1029/2023JD038827

Herlingshaw et al (2025) Science highlights from the Kjell Henriksen Observatory on Svalbard. Arctic Sci 11:1–25. https://doi.org/10.1139/as-2024-0009

Hibbins RE, Espy PJ, Orsolini YJ, Limpasuvan V, Barnes RJ (2019) SuperDARN observations of semidiurnal tidal variability in the MLT and the response to sudden stratospheric warming events. J Geophys Res Atmos 124:4862–4872. https://doi.org/10.1029/2018JD030157

Hitchman MH, Gille JC, Rodgers CD, Brasseur G (1989) The separated polar winter Stratopause: a gravity wave driven climatological feature. J Atmos Sci. https://doi.org/10.1175/1520-0469(1989)046<0410:TSPWSA>2.0.CO;2

Hocke K (2023) Influence of sudden stratospheric warmings on the migrating diurnal tide in the equatorial middle atmosphere observed by Aura/Microwave Limb Sounder. Atmosphere 14(12):1743. https://doi.org/10.3390/atmos14121743

Holmen S, Dyrland M, Sigernes F (2014) Mesospheric temperatures derived from three decades of hydroxyl airglow measurements from Longyearbyen, Svalbard (78°N, 15°E). Acta Geophys 62:302–315. https://doi.org/10.2478/s11600-013-0159-4

Holton JR (1983) The influence of gravity wave breaking on the general circulation of the Middle Atmosphere. J Atmos Sci. https://doi.org/10.1175/1520-0469(1983)040<2497:TIOGWB>2.0.CO;2

Holton JR (2004) An introduction to dynamic meteorology, 4th edn. Elsevier Academic Press, New York

Jacobi C, Fröhlich K, Viehweg C, Stober G, Kürschner D (2007) Midlatitude mesosphere/lower thermosphere meridional winds and temperatures measured with meteor radar. Adv Space Res 39:1278–1283. https://doi.org/10.1016/j.asr.2007.01.003

Jin H, Miyoshi Y, Pancheva D, Mukhtarov P, Fujiwara H, Shinagawa H (2012) Response of migrating tides to the stratospheric sudden warming in 2009 and their effects on the ionosphere studied by a whole atmosphere-ionosphere model GAIA with COSMIC and TIMED/SABER observations. J Geophys Res Space Phys. https://doi.org/10.1029/2012JA017650

Jones M Jr. et al (2020) Coupling from the middle atmosphere to the exobase: dynamical disturbance effects on light chemical species. J Geophys Res Space Phys. https://doi.org/10.1029/2020JA028331

Jucker M, Reichler T, Waugh DW (2021) How frequent are Antarctic sudden stratospheric warmings in present and future climate? Geophys Res Lett 48:e2021GL093215. https://doi.org/10.1029/2021GL093215

Karlsson B, McLandress C, Shepherd TG (2009) Inter-hemispheric mesospheric coupling in a comprehensive middle atmosphere model. J Atmos Solar Terr Phys 71:518–530. https://doi.org/10.1016/j.jastp.2008.08.006

Karlsson B, Becker E (2016) How does interhemispheric coupling contribute to cool down the summer polar mesosphere? J Climate 29(24):8807–8821. https://doi.org/10.1175/JCLI-D-16-0231.1

Kidston J, Scaife AA, Hardiman SC, Mitchell DM, Butchart N, Baldwin MP, Gray LJ (2015) Stratospheric influence on tropospheric jet streams, storm tracks and surface weather. Nat Geosci 8:433–440. https://doi.org/10.1038/ngeo2424

Kiefer M et al (2021) IMK/IAA MIPAS temperature retrieval version 8: nominal measurements. Atmos Meas Tech 14:4111–4138. https://doi.org/10.5194/amt-14-4111-2021

Kirner O, Ruhnke R, Sinnhuber BM (2015) Chemistry-climate interactions of stratospheric and mesospheric ozone in EMAC long-term simulations with different boundary conditions for CO_2, CH_4, N_2O, and ODS. Atmos Ocean 53(1):140–152. https://doi.org/10.1080/07055900.2014.980718

Kunze M, Zülicke C, Siddiqui TA, Stephan CC, Yamazaki Y, Stolle C, Borchert S, Schmidt H (2024) UA-ICON with NWP physics package (version: ua-icon-2.1): mean state and variability of the middle atmosphere. . https://doi.org/10.5194/gmd-2024-191Model Dev Discuss, Geosci.

Labitzke K (1972) Temperature changes in the mesosphere and stratosphere connected with circulation changes in winter. J Atmos Sci 29:756–766. https://doi.org/10.1175/1520-0469(1972)029%3c0756:TCITMA%3e2.0.CO;2

Langematz U, Kunze M, Kruger K, Labitzke K, Roff GL (2003) Thermal and dynamical changes of the stratosphere since 1979 and their link to ozone and CO_2 changes. J Geophys Res 108(D1):4027. https://doi.org/10.1029/2002JD002069

Laskar FI, McCormack JP, Chau JL, Pallamraju D, Hoffmann P, Singh RP (2019) Interhemispheric meridional circulation during sudden stratospheric warming. J Geophys Res Space Phys 124(8):7112–7122. https://doi.org/10.1029/2018JA026424

Liang Y-C et al (2024) The weakening of the stratospheric polar vortex and the subsequent surface impacts as consequences to Arctic sea ice loss. J Climate. https://doi.org/10.1175/JCLI-D-23-0128.1

Lieberman RS, Riggin DM, Franke SJ, Manson AH, Meek C, Nakamura T, Tsuda T, Vincent RA, Reid I (2003) The 6.5-day wave in the mesosphere and lower thermosphere: evidence for baroclinic/barotropic instability. J Geophys Res. https://doi.org/10.1029/2002JD003349

Lieberman RS, Riggin DM, Ortland DA, Oberheide J, Siskind DE (2015) Global observations and modeling of nonmigrating diurnal tides generated by tide-planetary wave interactions. J Geophys Res Atmos 120:11419–11437. https://doi.org/10.1002/2015JD023739

Lieberman RS, France JA, Ortland DA, Eckermann SD (2021) The role of inertial instability in cross-hemispheric coupling. J Atmos Sci 78(4):1113–1127. https://doi.org/10.1175/JAS-D-20-0119.1

Limpasuvan V, Orsolini YJ, Chandran A, Garcia RR, Smith AK (2016) On the composite response of the MLT to major sudden stratospheric warming events with elevated stratopause. J Geophys Res Atmos 121:4518–4537. https://doi.org/10.1002/2015JD024401

Lin CY, Matsuo T, Liu JY, Lin CH, Huba JD, Tsai HF, Chen CY (2017) Data assimilation of ground-based GPS and radio occultation total electron content for global ionospheric specification. J Geophys Res Space Phys 122(10):10–876. https://doi.org/10.1002/2017JA024185

Lindzen RS (1981) Turbulence and stress owing to gravity wave and tidal breakdown. J Geophys Res 86(C10):9707–9714. https://doi.org/10.1029/JC086iC10p09707

Liu G, Janches D, Lieberman RS, Moffat-Griffin T, Mitchell NJ, Kim J-H, Lee C (2021) Wind variations in the mesosphere and lower thermosphere near 60°S latitude during the 2019 Antarctic sudden stratospheric warming. J Geophys Res: Space Phys 126:e2020JA028909. https://doi.org/10.1029/2020JA028909

Liu H-L, Roble RG (2002) A study of a self-generated stratospheric sudden warming and its mesospheric-lower thermospheric impacts using the coupled TIME-GCM/CCM3. J Geophys Res 107(D23):4695. https://doi.org/10.1029/2001JD001533

Liu H-L (2017) Gravity wave variation from the troposphere to the lower thermosphere during a stratospheric sudden warming event: a case study. SOLA 13A:24–30. https://doi.org/10.2151/sola.13A-005

Liu H-L, Lauritzen PH, Vitt F, Goldhaber S (2024) Assessment of gravity waves from tropopause to thermosphere and ionosphere in high-resolution WACCM-X simulations. J Adv Model Earth Syst 16:e2023MS004024. https://doi.org/10.1029/2023MS004024

Livesey NJ, Filipiak MJ, Froidevaux L, Read WG, Lambert A, Santee ML et al (2008) Validation of aura microwave limb sounder O_3 and CO observations in the upper troposphere and lower stratosphere. J Geophys Res 113:D15S02. https://doi.org/10.1029/2007JD008805

Livesey NJ, Read WG, Wagner PA, Froidevaux L, Santee M et al (2020) Earth observing system (EOS) aura microwave limb sounder (MLS) version 5.0X Level 2 and 3 data quality and description document, Rep. JPL D-105336 Rev. A, Jet Propul. Lab., Pasadena, CA

Ma Z, Gong Y, Zhang S, Xiao Q, Huang C, Huang K (2024) Quasi-5-day oscillations during Arctic major sudden stratospheric warmings from 2005 to 2021. J Geophys Res Space Phys 129:e2023JA032292. https://doi.org/10.1029/2023JA032292

Maliniemi V, Marsh DR, Tyssøy HN, Smith-Johnsen C (2020) Will climate change impact polar NO_x produced by energetic particle precipitation? Geophys Res Lett 47:e2020GL087041. https://doi.org/10.1029/2020GL087041

Maliniemi V, Nesse Tyssøy H, Smith-Johnsen C, Arsenovic P, Marsh DR (2021) Effects of enhanced downwelling of NO_x on Antarctic upper-stratospheric ozone in the 21st century. Atmos Chem Phys 21:11041–11052. https://doi.org/10.5194/acp-21-11041-2021

Maliniemi V, Arsenovic P, Seppälä A, Nesse Tyssøy H (2022) The influence of energetic particle precipitation on Antarctic stratospheric chlorine and ozone over the 20th century. Atmos Chem Phys 22:8137–8149. https://doi.org/10.5194/acp-22-8137-2022

Manabe (1967) https://doi.org/10.1175/1520-0469(1967)024<0241:TEOTAW>2.0.CO;2

Manney GL et al (2008) The evolution of the stratopause during the 2006 major warming: data and assimilated meteorological analyses. J Geophys Res 113:D11115. https://doi.org/10.1029/2007JD009097

Manney GL et al (2009) Aura Microwave Limb Sounder observations of dynamics and transport during the record-breaking 2009 Arctic stratospheric major warming. Geophys Res Lett 36:L12815. https://doi.org/10.1029/2009GL038586

Matsuno T (1970) Vertical propagation of stationary planetary waves in the winter northern hemisphere. J Atmos Sci 37:871–883. https://doi.org/10.1175/1520-0469(1970)027%3c0871:VPOSPW%3e2.0.CO;2

McInturff RM (ed) (1978) Stratospheric warmings: synoptic, dynamic and general-circulation aspects. NASA Reference Publ. NASA-RP-1017. Available online at http://ntrs.nasa.gov/archive/nasa/casi.ntrs.nasa.gov/19780010687.pdf

McIntyre ME, Palmer TN (1984) The "surf zone" in the stratosphere. J Atmos Terr Phys 46:825–849. https://doi.org/10.1016/0021-9169(84)90063-1

McLandress C, Ward WE, Fomichev VI, Semeniuk K, Beagley SR, McFarlane NA, Shepherd TG (2006) Large-scale dynamics of the mesosphere and lower thermosphere: an analysis using the extended Canadian Middle Atmosphere Model. J Geophys Res 111:D17111. https://doi.org/10.1029/2005JD006776

McPeters RD (1980) The behavior of ozone near the stratopause from two years of BUV observations. J Geophys Res 85:4545–4550. https://doi.org/10.1029/JC085iC08p04545

Miyoshi Y, Fujiwara H, Jin H, Shinagawa H (2015) Impacts of sudden stratospheric warming on general circulation of the thermosphere. J Geophys Res Space Phys. https://doi.org/10.1002/2015JA021894

Molod A, Takacs L, Suarez M, Bacmeister J (2015) Development of the GEOS-5 atmospheric general circulation model: evolution from MERRA to MERRA2. Geosci Model Dev 8:1339–1356. https://doi.org/10.5194/gmd-8-1339-2015

Mošna Z, Edemskiy I, Laštovicka J, Kozubek M, Koucká Knížová P, Kouba D, Siddiqui TA (2021) Observation of the Ionosphere in Middle Latitudes during 2009, 2018 and 2018/2019 Sudden Stratospheric Warming Events. Atmosphere 12:602. https://doi.org/10.3390/atmos12050602

Myrabø HK (1984) Temperature variation at mesopause levels during winter solstice at 78°N. Planet Space Sci 32(2):249–255. https://doi.org/10.1016/0032-0633(84)90159-4

Myrabø HK, Deehr CS, Lybekk B (1984) Polar cap oh airglow rotational temperatures at the mesopause during a stratospheric warming event. Planet Space Sci 32(7):853–856. https://doi.org/10.1016/0032-0633(84)90009-6

Oberheide J, Pedatella NM, Gan Q, Kumari K, Burns AG, Eastes RW (2020) Thermospheric composition O/N_2 response to an altered meridional mean circulation during sudden stratospheric warmings observed by GOLD. Geophys Res Lett. https://doi.org/10.1029/2019GL086313

Orsolini YJ, Limpasuvan V, Pérot K, Espy P, Hibbins R, Lossow S, Larsson KR, Murtagh D (2017) Modelling the descent of nitric oxide during the elevated stratopause event of January 2013. J Atmos Solar Terr Phys 155:50–61. https://doi.org/10.1016/j.jastp.2017.01.006

O'Sullivan D, Dunkerton TJ (1995) Generation of inertia-gravity waves in a simulated life cycle of Baroclinic instability. J Atmos Sci 52(21):3695–3716. https://doi.org/10.1175/1520-0469(1995)052%3c3695:GOIWIA%3e2.0.CO;2

Pancheva D, Mukhtarov P (2011) Atmospheric tides and planetary waves: recent progress based on SABER/TIMED temperature measurements (2002–2007). In: Abdu M, Pancheva D (eds) Aeronomy of the Earth's Atmosphere and Ionosphere. IAGA Special Sopron Book Series, vol 2. Springer, Dordrecht. https://doi.org/10.1007/978-94-007-0326-1_2

Pedatella NM, Liu HL, Richmond AD, Maute A, Fang TW (2012) Simulations of solar and lunar tidal variability in the mesosphere and lower thermosphere during sudden stratosphere warmings and their influence on the low-latitude ionosphere. J Geophys Res: Space Phys. https://doi.org/10.1029/2012JA017858

Pedatella NM, Liu H-L, Sassi F, Lei J, Chau JL, Zhang X (2014) Ionosphere variability during the 2009 SSW: Influence of the lunar semidiurnal tide and mechanisms producing electron density variability. J Geophys Res Space Physics 119:3828–3843. https://doi.org/10.1002/2014JA019849

Pedatella NM, Liu H-L, Marsh DR, Raeder K, Anderson JL, Chau JL et al (2018a) Analysis and hindcast experiments of the 2009 sudden stratospheric warming in WACCMX+DART. J Geophys Res Space Physics 123:3131–3153. https://doi.org/10.1002/2017JA025107

Pedatella NM, Chau JL, Schmidt H, Goncharenko LP, Stolle C, Hocke K, Harvey VL, Funke B, Siddiqui TA (2018b) Sudden stratospheric warming impacts on the whole atmosphere. Eos. https://doi.org/10.1020/2017ES005448

Pedatella NM, Harvey VL (2022) Impact of strong and weak stratospheric polar vortices on the mesosphere and lower thermosphere. Geophys Res Lett. https://doi.org/10.1029/2022GL098877

Plougonven R, Zhang F (2014) Internal gravity waves from atmospheric jets and fronts. Rev Geophys 52:33–76. https://doi.org/10.1002/2012RG000419

Pumphrey HC, Filipiak MJ, Livesey NJ, Schwartz MJ, Boone C, Walker KA et al (2007) Validation of middle-atmosphere carbon monoxide retrievals from the Microwave Limb Sounder on Aura. J Geophys Res 112:D24S38. https://doi.org/10.1029/2007JD008723

Quiroz RS (1969) The warming of the upper stratosphere in February 1966 and the associated structure of the mesosphere. Mon Weather Rev 97(8):541–552. https://doi.org/10.1175/1520-0493(1969)097%3c0541:TWOTUS%3e2.3.CO;2

Randall CE, Harvey VL, Siskind DE, France JA, Bernath PF, Boone CD, Walker KA (2009) NO_x descent in the Arctic middle atmosphere in early 2009. Geophys Res Lett. https://doi.org/10.1029/2009GL039706

Randel WJ (1993) Global variations of zonal mean zonal ozone during stratospheric warming events. J Atmos Sci 50:3308–3321. https://doi.org/10.1175/1520-0469(1993)050%3c3308:GVOZMO%3e2.0.CO;2

Randel WJ et al (2009) An update of observed stratospheric temperature trends. J Geophys Res 114:D02107. https://doi.org/10.1029/2008JD010421

Reinisch BW, Galkin IA (2011) Global Ionospheric Radio Observatory (GIRO). Earth Planet Space 63:377–381. https://doi.org/10.5047/eps.2011.03.001

Russell III JM, Mlynczak MG, Gordley LL, Tansock Jr, JJ, Esplin RW (1999) Overview of the SABER experiment and preliminary calibration results. Optical spectroscopic techniques and instrumentation for atmospheric and space research III 3756:277–288. https://doi.org/10.1117/12.366382

Santer BD, Po-Chedley S, Zhao L, Taylor KE (2023) Exceptional stratospheric contribution to human fingerprints on atmospheric temperature. Proc Natl Acad Sci USA. https://doi.org/10.1073/pnas.2300758120

Sato K, Yoshiki M (2008) Gravity wave generation around the polar vortex in the stratosphere revealed by 3-hourly radiosonde observations at Syowa Station. J Atmos Sci 65(12):3719–3735. https://doi.org/10.1175/2008JAS2539.1

Schmidt C, Höppner K, Bittner M (2013) A ground-based spectrometer equipped with an InGaAs array for routine observations of OH(3-1) rotational temperatures in the mesopause region. J Atmos Solar Terr Phys 102:125–139. https://doi.org/10.1016/j.jastp.2013.05.001

Schmidt C, Küchelbacher L, Wüst S, Bittner M (2023) Oh airglow observations with two identical spectrometers: benefits of increased data homogeneity in the identification of variations induced by the 11-year solar cycle, the QBO, and other factors. Atmos Meas Tech 16(19):4331–4356. https://doi.org/10.5194/amt-16-4331-2023

Schoeberl MR, Lait LR, Newman PA, Rosenfield JE (1992) The structure of the polar vortex. J Geophys Res Atmos 97(D8):7859–7882. https://doi.org/10.1029/91JD02168

Schranz F, Fernandez S, Kämpfer N, Palm M (2018) Diurnal variation in middle-atmospheric ozone observed by ground-based microwave radiometry at Ny-Ålesund over 1 year. Atmos Chem Phys 18:4113–4130. https://doi.org/10.5194/acp-18-4113-2018

Schranz F, Tschanz B, Rüfenacht R, Hocke K, Palm M, Kämpfer N (2019) Investigation of Arctic middle-atmospheric dynamics using 3 years of H_2O and O_3 measurements from microwave radiometers at Ny-Ålesund. Atmos Chem Phys 19:9927–9947. https://doi.org/10.5194/acp-19-9927-2019

Schranz F, Hagen J, Stober G, Hocke K, Murk A, Kämpfer N (2020) Small-scale variability of stratospheric ozone during the sudden stratospheric warming 2018/2019 observed at Ny-Ålesund, Svalbard. Atmos Chem Phys 20:10791–10806. https://doi.org/10.5194/acp-20-10791-2020

Schwartz MJ, Read WG, Livesey NJ, Froidevaux L, Santee ML et al (2008) Validation of the Aura Microwave Limb Sounder temperature and geopotential height measurements. J Geophys Res 113:D15S11. https://doi.org/10.1029/2007JD008783

Seviour WJM, Mitchell DM, Gray LJ (2013) A practical method to identify displaced and split stratospheric polar vortex events. Geophys Res Lett 40:5268–5273. https://doi.org/10.1002/grl.50927

Shi G, Krochin W, Sauvageat E, Stober G (2023) Ozone and water vapor variability in the polar middle atmosphere observed with ground-based microwave radiometers. Atmos Chem Phys 23:9137–9159. https://doi.org/10.5194/acp-23-9137-2023

Shi G, Krochin W, Sauvageat E, Stober G (2024) Ozone anomalies over the polar regions during stratospheric warming events. Atmos Chem Phys 24:10187–10207. https://doi.org/10.5194/acp-24-10187-2024

Siddiqui TA, Maute A, Pedatella NM (2019) On the importance of interactive ozone chemistry in Earth-system models for studying mesosphere-lower thermosphere tidal changes during sudden stratospheric warmings. J Geophys Res Space Phys 124:10690–10707. https://doi.org/10.1029/2019JA027193

Siddiqui TA, Chau JL, Stolle C, Yamazaki Y (2022) Migrating solar diurnal tidal variability during northern and southern hemisphere sudden stratospheric warmings. Earth Planets Space 74(1):101. https://doi.org/10.1186/s40623-022-01661-y

Sigernes F, Shumilov N, Deehr CS, Nielsen KP, Svenøe T, Havnes O (2003) Hydroxyl rotational temperature record from the auroral station in Adventdalen, Svalbard (78°N, 15°E). J Geophys Res Space Phys 108:1342. https://doi.org/10.1029/2001JA009023

Siskind DE et al (2010) Case studies of the mesospheric response to recent minor, major, and extended stratospheric warmings. J Geophys Res 115:D00N03. https://doi.org/10.1029/2010JD014114

Smith AK, Marsh DR, Mlynczak MG, Mast JC (2010) Temporal variations of atomic oxygen in the upper mesosphere from SABER. J Geophys Res 115:D18309. https://doi.org/10.1029/2009JD013434

Smith AK, Pedatella NM, Mullen ZK (2020) Interhemispheric coupling mechanisms in the middle atmosphere of WACCM6. J Atmos Sci 77(3):1101–1118. https://doi.org/10.1175/JAS-D-19-0253.1

Stober G, Jacobi C, Matthias V, Hoffmann P, Gerding M (2012) Neutral air density variations during strong planetary wave activity in the mesopause region derived from meteor radar observations. J Atmos Sol-Terr Phys 74:55–63. https://doi.org/10.1016/j.jastp.2011.10.007

Stober G, Baumgarten K, McCormack JP, Brown P, Czarnecki J (2020) Comparative study between ground-based observations and NAVGEM-HA analysis data in the mesosphere and lower thermosphere region. Atmos Chem Phys 20:11979–12010. https://doi.org/10.5194/acp-20-11979-2020

Stober G et al (2021a) Atmospheric tomography using the Nordic Meteor Radar Cluster and Chilean Observation Network De Meteor Radars: network details and 3D-Var retrieval. Atmos Meas Tech 14:6509–6532. https://doi.org/10.5194/amt-14-6509-2021

Stober G et al (2021b) Interhemispheric differences of mesosphere–lower thermosphere winds and tides investigated from three whole-atmosphere models and meteor radar observations. Atmos Chem Phys 21:13855–13902. https://doi.org/10.5194/acp-21-13855-2021

Stober G et al (2022) Meteor radar vertical wind observation biases and mathematical debiasing strategies including the 3DVAR+DIV algorithm. Atmos Meas Tech 15:5769–5792. https://doi.org/10.5194/amt-15-5769-2022

Straub C, Tschanz B, Hocke K, Kämpfer N, Smith AK (2012) Transport of mesospheric H_2O during and after the stratospheric sudden warming of January 2010: observation and simulation. Atmos Chem Phys 12:5413–5427. https://doi.org/10.5194/acp-12-5413-2012

Stray NH, Orsolini YJ, Espy PJ, Limpasuvan V, Hibbins RE (2015) Observations of planetary waves in the mesosphere-lower thermosphere during stratospheric warming events. Atmos Chem Phys 15:4997–5005. https://doi.org/10.5194/acp-15-4997-2015

Teitelbaum H, Vial F (1991) On tidal variability induced by nonlinear interaction with planetary waves. J Geophys Res 96:14,169-14,178. https://doi.org/10.1029/91JA01019

Trinh QT, Ern M, Doornbos E, Preusse P, Riese M (2018) Satellite observations of middle atmosphere–thermosphere vertical coupling by gravity waves. Ann Geophys 36:425–444. https://doi.org/10.5194/angeo-36-425-2018

Tweedy OV et al (2013) Nighttime secondary ozone layer during major stratospheric sudden warmings in specified-dynamics WACCM. J Geophys Res Atmos 118:8346–8358. https://doi.org/10.1002/jgrd.50651

Vadas SL, Becker E, Bossert K, Baumgarten G, Hoffmann L, Harvey VL (2023) Secondary gravity waves from the stratospheric polar vortex over ALOMAR observatory on 12–14 January 2016: observations and modeling. J Geophys Res Atmos 128:e2022JD036985. https://doi.org/10.1029/2022JD036985

Vadas SL, Becker E, Bossert K, Hozumi Y, Stober G, Harvey VL, Randall CE, Baumgarten G, Hoffmann L, Yue J (2024a) The role of the polar vortex jet for secondary and higher-order gravity waves in the northern mesosphere and thermosphere during 11–14 January 2016. JGR Atmos. https://doi.org/10.1029/2024JA032521

Vadas SL, Themens D, Huba JD, Becker E, Goncharenko L, Bossert K, Figueiredo C, Xu S, Harvey VL (2024b) Higher-order gravity waves and traveling ionospheric disturbances from the polar vortex jet on 11–15 January 2016: modeling with HIAMCM-SAMI3 and comparison with observations in the thermosphere and ionosphere. JGR Space Phys. https://doi.org/10.1029/2024JA033040

van Caspel WE, Espy PJ, Hibbins RE, McCormack JP (2020) Migrating tide climatologies measured by a high-latitude array of SuperDARN HF radars. Ann Geophys 38:1257–1265. https://doi.org/10.5194/angeo-38-1257-2020

van Caspel WE, Espy PJ, Ortland DA, Hibbins RE (2022) The mid- to high-latitude migrating semidiurnal tide: results from a mechanistic tide model and SuperDARN observations. J Geophys Res Atmos 127:e2021JD036007. https://doi.org/10.1029/2021JD036007

van Caspel WE, Espy P, Hibbins R, Stober G, Brown P, Jacobi C, Kero J (2023) A case study of the solar and lunar semidiurnal tide response to the 2013 sudden stratospheric warming. J Geophys Res Space Phys 128:e2023JA031680. https://doi.org/10.1029/2023JA031680

Vial F, Forbes JM, Miyahara S (1991) Some transient aspects of tidal propagation. J Geophys Res Space Phys 96(A2):1215–1224. https://doi.org/10.1029/90JA02181

Wang L, Alexander MJ (2009) Gravity wave activity during stratospheric sudden warmings in the 2007–2008 Northern Hemisphere winter. J Geophys Res 114:D18108. https://doi.org/10.1029/2009JD011867

Wang H, Akmaev RA, Fang TW, Fuller-Rowell TJ, Wu F, Maruyama N, Iredell MD (2014) First forecast of a sudden stratospheric warming with a coupled whole-atmosphere/ionosphere model IDEA. J Geophys Res Space Physics 119(3):2079–2089. https://doi.org/10.1002/2013JA019481

Warner CD, McIntyre ME (1996) On the propagation and dissipation of gravity wave spectra through a realistic middle atmosphere. J Atmos Sci 53(22):3213–3235. https://doi.org/10.1175/1520-0469(1996)053%3c3213:OTPADO%3e2.0.CO;2

Waters JW, Froidevaux L, Harwood RS, Jarnot RF, Pickett HM, Read WG et al (2006) The earth observing system microwave limb sounder (EOS MLS) on the Aura satellite. IEEE Trans Geosci Remote Sens 44(5):1075–1092. https://doi.org/10.1109/TGRS.2006.873771

Whiteway JA, Carswell AI (1994) Rayleigh lidar observations of thermal structure and gravity wave activity in the high arctic during a stratospheric warming. J Atmos Sci.

Whiteway JA, Duck TJ, Donovan DP, Bird JC, Pal SR, Carswell AI (1997) Measurements of gravity wave activity within and around the Arctic stratospheric vortex. Geophys Res Lett 24(11):1387–1390. https://doi.org/10.1029/97GL01322

Whiteway JA, Duck TJ (1999) Enhanced arctic stratospheric gravity wave activity above a tropospheric jet. Geophys Res Lett 26(16):2453–2456. https://doi.org/10.1029/1999GL900548

Wüst S et al (2017) Variability of the Brunt-Väisälä frequency at the OH* layer height. Atmos Meas Tech 10(12):4895–4903. https://doi.org/10.5194/amt-10-4895-2017

Wüst S et al (2020) Variability of the Brunt-Väisälä frequency at the OH*-airglow layer height at low and midlatitudes. Atmos Meas Tech 13(11):6067–6093. https://doi.org/10.5194/amt-13-6067-2020

Wüst S et al (2023) Hydroxyl airglow observations for investigating atmospheric dynamics: results and challenges. Atmos Chem Phys 23(2):1599–1618. https://doi.org/10.5194/acp-23-1599-2023

Yamashita C, Liu H-L, Chu X (2010) Gravity wave variations during the 2009 stratospheric sudden warming as revealed by ECMWF-T799 and observations. Geophys Res Lett 37:L22806. https://doi.org/10.1029/2010GL045437

Yamazaki Y, Kosch M-J, Emmert J-T (2015) Evidence for stratospheric sudden warming effects on the upper thermosphere derived from satellite orbital decay data during 1967–2013. Geophys Res Lett 42:6180–6188. https://doi.org/10.1002/2015gl065395

Yamazaki Y, Richmond AD, Liu H, Yumoto K, Tanaka Y (2012) Sq current system during stratospheric sudden warming events in 2006 and 2009. J Geophys Res Space Phys. https://doi.org/10.1029/2012JA018116

Yamazaki Y (2023) A method to derive Fourier–wavelet spectra for the characterization of global-scale waves in the mesosphere and lower thermosphere and its MATLAB and Python software (fourierwavelet v1. 1). Geosci Model Dev 16(16):4749–4766. https://doi.org/10.5194/gmd-16-4749-2023

Yamazaki Y, Siddiqui TA (2024) Symmetric and antisymmetric solar migrating semidiurnal tides in the mesosphere and lower thermosphere. J Geophys Res Atmos 129(12):e2023JD040222. https://doi.org/10.1029/2023JD040222

Yasyukevich A, Medvedeva I, Sivtseva V, Chernigovskaya M, Ammosov P, Gavrilyeva G (2020) Strong interrelation between the short-term variability in the ionosphere, upper mesosphere, and winter polar stratosphere. Remote Sens 12(10):1588. https://doi.org/10.3390/rs12101588

Yoshiki M, Sato K (2000) A statistical study of gravity waves in the polar regions based on operational radiosonde data. J Geophys Res Atmos 105(D14):17995–18011. https://doi.org/10.1029/2000JD900204

Yoshiki M, Kizu N, Sato K (2004) Energy enhancements of gravity waves in the Antarctic lower stratosphere associated with variations in the polar vortex and tropospheric disturbances. J Geophys Res Atmos. https://doi.org/10.1029/2004JD004870

Yue J, Lieberman R, Chang LC (2021) Planetary waves and their impact on the mesosphere, thermosphere, and ionosphere, upper atmosphere dynamics and energetics, Chapter 10. Editor(s): Wenbin Wang, Yongliang Zhang, Larry J. Paxton. https://doi.org/10.1002/9781119815631.ch10

Yulaeva E, Holton JR, Wallace JM (1994) On the cause of the annual cycle in tropical lower-stratospheric temperatures. J Atmos Sci 51(2):169–174. https://doi.org/10.1175/1520-0469(1994)051%3c0169:OTCOTA%3e2.0.CO;2

Zängl G, Reinert D, Ripodas P, Baldauf M (2015) The ICON (ICOsahedral non-hydrostatic) modelling framework of DWD and MPI-M: description of the non-hydrostatic dynamical core. Q J R Meteorol Soc. https://doi.org/10.1002/qj.2378

Zhang F (2004) Generation of mesoscale gravity waves in upper-tropospheric jet-front systems. J Atmos Sci 61(4):440–457. https://doi.org/10.1175/1520-0469(2004)061%3c0440:GOMGWI%3e2.0.CO;2

Zhang J, Limpasuvan V, Orsolini YJ, Espy PJ, Hibbins RE (2021) Climatological westward propagating semidiurnal tides and their composite response to sudden stratospheric warmings in SuperDARN and SD-WACCM-X. J Geophys Res Atmos 126:e2020JD032895. https://doi.org/10.1029/2020JD032895

Zhang J, Zhao Y, Pautet P-D, Scherliess L, Taylor MJ, Liu H (2025) Gravity wave activity during the 2024 sudden stratospheric warmings observed by atmospheric waves experiment (AWE). Geophys Res Lett 52:e2024GL114187. https://doi.org/10.1029/2024GL114187

Authors and Affiliations

V. L. Harvey[1] · **D. Aggarwal**[2] · **E. Becker**[3] · **M. Bittner**[4,5] · **B. Funke**[6] · **L. Goncharenko**[7] · **J. Jia**[8] · **R. Lieberman**[9] · **H.-L. Liu**[10] · **V. Maliniemi**[11] · **A. Marchaudon**[12] · **H. Nesse**[13] · **N. Partamies**[14] · **N. Pedatella**[10] · **C. Schmidt**[4] · **G. Shi**[15,16] · **C. C. Stephan**[17] · **G. Stober**[15,16] · **W. van Caspel**[18] · **S. Wüst**[4] · **Y. Yamazaki**[17]

✉ V. L. Harvey
lynn.harvey@lasp.colorado.edu

[1] Laboratory for Atmospheric and Space Physics, University of Colorado, Boulder, CO, USA

[2] Physics and Astronomy Department, Clemson University, Clemson, SC, USA

[3] Northwest Research Associates, Boulder, CO, USA

[4] German Remote Sensing Data Center, German Aerospace Center, Oberpfaffenhofen, Germany

[5] Institute of Physics, University of Augsburg, Augsburg, Germany

[6] Instituto de Astrofísica de Andalucía (CSIC), Granada, Spain

[7] MIT Haystack Observatory, Westford, MA, USA

[8] Department of Physics, Norwegian University of Science and Technology, Trondheim, Norway

[9] NASA Goddard Space Flight Center, Greenbelt, MD, USA

[10] High Altitude Observatory, NSF National Center for Atmospheric Research, Boulder, CO, USA

[11] Water, Energy, and Environmental Engineering Research Unit, University of Oulu, Oulu, Finland

[12] Institut de Recherche en Astrophysique et Planétologie, Université de Toulouse, CNRS, CNES, Toulouse, France

[13] Department of Physics and Technology, University of Bergen, Bergen, Norway

[14] Department of Arctic Geophysics, The University Centre in Svalbard, Longyearbyen, Svalbard, Norway

[15] Institute of Applied Physics, University of Bern, Bern, Switzerland

[16] Oeschger Center for Climate Change Research, University of Bern, Bern, Switzerland

[17] Leibniz Institute of Atmospheric Physics, University of Rostock, Kühlungsborn, Germany

[18] Climate Modelling and Air Pollution Division, Research and Development Department, Norwegian Meteorological Institute, Oslo, Norway